

**SYNERGY OF WIDE-FIELD INFRARED
SURVEY EXPLORER (WISE) AND THE
SLOAN DIGITAL SKY SURVEY IN STRIPE 82**

A Thesis presented to
the Faculty of the Graduate School
at the University of Missouri

In Partial Fulfillment
of the Requirements for the Degree
Doctor of Philosophy

by
MARAT MUSIN
Dr.Haojing Yan, Thesis Supervisor
MAY 2018

The undersigned, appointed by the Dean of the Graduate School, have examined
the Dissertation entitled:

SYNERGY OF WIDE-FIELD INFRARED
SURVEY EXPLORER (WISE) AND THE
SLOAN DIGITAL SKY SURVEY IN STRIPE 82

presented by Marat Musin,
a candidate for the degree of Doctor of Philosophy and hereby certify that, in their
opinion, it is worthy of acceptance.

Dr. Haojing Yan

Dr. Adam Helper

Dr. Angela Speck

Dr. Sergei Kopeikin

TABLE OF CONTENTS

LIST OF TABLES	vi
LIST OF FIGURES	vii
ABSTRACT	xii
CHAPTER	
1 Introduction	1
2 Data	5
2.1 SDSS	6
2.1.1 Stripe 82	6
2.1.2 Structure of SDSS Stripe 82 files	8
2.2 WISE	8
2.2.1 unWISE	9
2.2.2 Structure of unWISE files	9
3 Construction of the multiband catalog over Stripe 82	11
3.1 Preparatory work with SDSS images and optical catalog	13
3.1.1 Region of overlapping unWISE images	14
3.1.2 SDSS PSF construction	14
3.1.3 Construction of the optical part of the catalog	20
3.1.4 Magnitude error correction	21
3.2 Preparatory work with unWISE files	23
3.2.1 unWISE PSF construction	23
3.2.2 Naming convention for the processed files	24
3.3 Template fitting with TPHOT	24

3.3.1	TPHOT output files	27
3.4	Matching optical and IR catalogs	28
4	Mass and redshift estimation	29
4.1	SED fitting	31
4.1.1	Choice of SED fitting codes	31
4.1.2	EAZY and FAST	33
4.1.3	Reliability of IR data	34
4.1.4	Stellar masses	34
4.2	Catalog post-processing	37
4.2.1	Star-galaxy separation	37
4.2.2	Sources treatment in overlapping regions and around bright stars	40
5	Results	45
5.1	Binning in redshift	45
5.2	GSMD and comparison to the results of other groups	47
6	Summary and concluding remarks	50
6.1	Conclusions	50
6.2	Future work	51
6.2.1	Optical dropouts in WISE	53
ACKNOWLEDGMENTS		ii
APPENDIX		iii
A	Parameters for applied codes	iii
A.1	Sextractor parameters for x_matched_u catalogs	iii
A.2	TPHOT parameters	v
A.3	EAZY parameters	vii
A.4	FAST parameters	viii

BIBLIOGRAPHY	x
------------------------	---

LIST OF TABLES

Table	Page
3.1 Table of parameters for selection of PSF stars	16
3.2 Table of parameters for <code>IRAF/psf</code> task.	17
5.1 Redshift binning of stellar mass	46
5.2 Stellar mass density	46

LIST OF FIGURES

Figure	Page
2.1 The camera used for imaging. It consists of 30 photometric CCDs, that are arranged in 6 columns of 5 each. Camera is drifted in the way that each column has permanent Declination during the run and all 5 filters in a column consequently go over the same field	7
3.1 Optical catalogs from J14 (denoted with green circles) and our catalog (red circles) are overplotted on a small random area in Stripe 82. There is a number of well-detected sources that were excluded from J14 catalog and also there are multiple detections around a saturated source in the upper part of the plot. Our catalog aims to resolve both such issues.	12
3.2 A set of PSFs for five bands for odd columns centered at RA=21:56:46. All PSFs are scaled to the unit flux	18
3.3 An example of <code>IRAF/psfmatch</code> for <i>griz</i> bands (top to bottom). Original images are to the left, PSF-matched - to the right. The difference is mostly observable for r- and i-bands, because their PSF is much better than that in u-band	19
3.4 An example of the change in magnitude error for r-band photometry. Original errors are plotted against AB mag in red, magnitude errors for the same source after <code>IRAF/psfmatch</code> is performed are in blue. . .	21

3.5	Correction coefficients for all 5 bands for two columns - col04 (top) and col12 (bottom). Note that coefficients for the u-band are less than one	22
3.6	unWISE PSFs for w1 (top row) and w2 bands (bottom row), as constructed in <code>IRAF/psf</code> (left) and scaled by factor x7 to mimic pixel scale ratio between SDSS and unWISE pixel scales (right)	25
3.7	From left to right: SDSS image in r-band, unWSIE w1 image, residual image from <code>TPHOT</code> . SDSS sources that are fitted to the unWISE image for the flux estimation are denoted with red circles. These objects are cleaned out from the residual image	27
4.1	Comparison of <code>photo_z</code> as calculated in EAZY to the <code>spec_z</code> from the SDSS spectroscopic data. <code>Photo_z</code> vs <code>spec_z</code> is plotted on top, another version of this plot, <code>photo_z - spec_z</code> vs <code>spec_z</code> is plotted at the bottom. Despite several observable issues (especially around $z \approx 0.4$ the overall fit is satisfying with the standard deviation as low as $\sigma = 0.07$	35
4.2	Difference of <code>photo_z</code> and <code>spec_z</code> is plotted against <code>spec_z</code> . Data obtained with all 7 or just 5 optical filters are plotted in red and green respectively.	36
4.3	A histogram of masses for all four redshift bins. Galaxies in different bins end to peak at different masses, but galaxies in three high-redshift bins have the highest number of galaxies around similar stellar mass - 10^{10}	37
4.4	Color-color diagram for star-galaxy separation using " $w1 - i$ vs $i - z$ " colors. Galaxies are plotted in blue, stars - in red and QSO in green. It is impossible to create a clean data sample using only colors as a selection criteria.	38

4.5 A histogram of the CLASS_STAR values for r-band alone already shows efficiency of this method for star-galaxy separation. Galaxies and stars are selected from BOSS spectroscopic survey using parameter "CLASS". Galaxies are plotted in blue and tend to have smaller values of CLASS_STAR, stars are plotted in green and on opposite - mostly have CLASS_STAR value close to 1.	40
4.6 A histogram of the CLASS_STAR values for galaxies from the control data sample that are rejected from our data sample due to very large CLASS_STAR values (green). In red we plotted stars and QSO that are not excluded from our data sample - their CLASS_STAR values are too small in all three optical bands that we used for star-galaxy separation.	40
4.7 Duplicate sources (blue) are over-plotted with unique sources (red) in one unWISE frame that hosts 72 SDSS images (top image) and several adjacent unWISE frames (bottom image). Two white horizontal stripes between col07 and col02 (bottom) and coll11 and col06 (top) were also excluded from our project.	43
4.8 Residual image in w1 band with various regions plotted. All sources that were detected in r-band and supplied to TPHOT, but fall within the masked region (red) are excluded from the SED fitting. Blue circles 3 asec in radius show the position of objects, whose flux was subtracted from the unWISE image. Poorly subtracted objects (mostly stars) without blue circles around them were included into TPHOT input catalog, but later were excluded from ED fitting after star-galaxy separation	44

5.1 Stellar mass density over photometric redshift. Four reddshift bins are plotted in different colors: z1 - blue, z2 - green, z3 - grey, z4 - magenta. Red sources at $z > 0.759$ are not included into the sample due to their low number density.	46
5.2 Stellar masses are plotted over corresponding r-band magnitudes. Four redshift bins are plotted in different colors: z1 - blue, z2 - green, z3 - grey, z4 - magenta. Red vertical line denotes the 3σ detection limit.	47
5.3 Figure 11 from Madau&Dickinson. 2014 with our SMD data points plotted as low-limit with green dots with arrows. Data points inside the red rectangular demonstrate an odd "wiggle" upwards as if the SMD was higher in the earlier Universe	49
6.1 Stellar masses are plotted over corresponding w1-band magnitudes. Four redshift bins are plotted in different colors: z1 - blue, z2 - green, z3 - grey, z4 - magenta. Black vertical line denotes the 5σ detection limit for unWISE, red vertical image - analogous detection limit for the stacked WISE and NEOWISER data	52
6.2 An example of WoDrop. Shown from left to right are the <i>ugriz</i> and unWISE w1 and w2 images. The images are $33''33''$ in size, and the green circles indicate the location of the WoDrop. For this particular example is $\text{SNR} = 8$ and 5.4 for bands w1 and w2 respectively.	53
6.3 Illustration of the probable explanation to the nature of WoDrops. The photometry of this object in w1 and w2 are indicated by the two magenta points, and its non-detection in the Stripe 82 <i>ugriz</i> images is indicated by the 2σ upper limits shown in grey.	54

6.4 An example of two WoDrops that have been observed by near-IR imager WHIRC instrument at WIYN telescope. All images are 33”33” in size, and the red circles indicate the location of the WoDrop. The nominal on-source exposures are 31 min, 43 min and 1.1 hrs in Ks, but as can be seen, one WoDrop is only detected in H and Ks band, while the second one is not detected (as well as other three WoDrops that were observed in this run)	55
--	----

ABSTRACT

In this dissertation, I aim to study the evolution of galaxies over the last 6 Gyr by measuring the growth of the global stellar mass density (GSMD) since $z = 0.8$. My work combines the datasets from two very large surveys, namely, the optical data from the Sloan Digital Sky Survey (SDSS) Stripe 82 and the infrared data from the Wide-field Infrared Survey Explorer (WISE), and constructs a unique catalog of galaxies that have their spectral energy distributions (SEDs) measured consistently from 0.3 to $5 \mu\text{m}$ in seven bands. This catalog, the largest of its kind, contains 9 million galaxies in $\sim 300 \deg^2$, will have a wide range of applications beyond the scope of this thesis.

Extending galaxy SED measurements to restframe near-IR has two significant advantages: (1) dust extinction can be better handled, and (2) emissions from low-mass stars, which are the major contributors to a galaxy's stellar mass, can be better measured. WISE was the only mission to date that provided all-sky IR data that are deep enough for galaxy evolution studies out to $z \approx 1$ (sampling restframe K-band). The only wide-field optical survey data that could match WISE depths are those from the SDSS Stripe 82 over $\sim 300 \deg^2$. The synergy of the two is therefore natural. The implementation, however, is of tremendous difficulty. This is mainly because of the vastly different spatial resolutions between SDSS and WISE. To overcome this problem, we take an approach that is often referred to as "morphological template fitting", i.e., using the high-resolution image to define the morphological template of the galaxy in question, and de-convolving its light profile in the low-resolution image accordingly. In this way, we obtain the SED measurements over the entire $0.3\text{-}5\mu\text{m}$ range in the most self-consistent manner. Using this SED catalog as the basis, we derive photometric redshifts and stellar masses for all the 9 million galaxies that span

$z = 0\text{--}0.8$. This provides us an unprecedented statistics when deriving galaxy stellar mass functions (MFs) and GSMD over multiple redshift bins. Some preliminary results are discussed.

As a by-product of our morphological template fitting process, an interesting population of objects called "WISE Optical Dropouts" ("WoDrops" for short) are discovered. These objects are significant detections in WISE data but are invisible in all the SDSS Stripe 82 data. Their nature remains a mystery up to this point. Among all possibilities, the only viable interpretation is that they are very high-mass galaxies with very high dust extinctions. To reveal their nature, future observations at larger facilities will be necessary.

Chapter 1

Introduction

Evolution of galaxies is a one of the key topics in modern astrophysics. In our currently accepted cosmological model, dark matter halos (where galaxies and galaxy clusters have been formed and reside till now) are built up via hierarchical merging process. The physics of galaxy formation is much more complicated and involves gas interaction, stellar formation and various feedback processes (such as those due to supernovae and active galactic nuclei). Over last two decades Lilly-Madau [Lilly et al., 1996], [Madau et al., 1996] diagram was in the center of discussion - it shows that the star formation rate density (SFRD) in the Universe was increasing as we go to higher redshifts, peaks at $z \sim 1$ and then decreases beyond that. Started with only seven data points, three of which were low-limits, it was soon complemented by high-z data from a variety of data (e.g. [Bouwens et al., 2004a], [Bouwens et al., 2004b], [Bunker et al., 2004]), most of which used Hubble Ultra-Deep field (UDF). While this diagram is still a widely-used tool to explain galaxy evolution, it is subject to uncertainties associated with robust estimation and calibration of star formation rates (SFR), effects of dust on SFR estimates, relatively poor sensitivity for most SFR indicators, and field-to-field variations caused by large scale structure (especially in a very narrow deep fields like UDF). For these reason it would be useful to have an

independent way to understand star formation history of the Universe.

Global stellar mass density (GSMD), which quantifies the growth of the amount of baryonic matter that is locked into stars in time, gives us such opportunity - it equals to the integral over the cosmic SFR, i.e. contains the same information about evolution of the galaxies (assuming correct choice of IMF), but suffers from completely different systematic uncertainties and is therefore an invaluable probe of the broad evolution of the stellar content of the Universe. Recent works by [Moustakas et al., 2013], [Bielby et al., 2012], [Bielby et al., 2012], [Muzzin et al., 2013] (more results are presented in a review paper by [Madau and Dickinson, 2014]) significantly contributed to our knowledge of the shape of GSMD up to redshifts $z \approx 8$. But the picture is not clear - the spread in results can reach up to 0.5 dex even in the local Universe ($z < 0.1$).

The main goal of this thesis is to derive GSMD at low redshifts (up to $z \sim 0.8$) using the largest sample possible to date. This is to be achieved by integrating the near-IR data from the Wide-field Infrared Survey Explorer (WISE) [Wright et al., 2010] and the deep optical data from the Sloan Digital Sky Survey in the Stripe 82 region, totaling ≈ 300 square degrees. We shall use unique approach to construct the most reliable spectral energy distribution (SED) spanning 0.35 to $4.6 \mu m$. This large sample (more than 9 million galaxies) will allow us to derive the GSMD in the low redshift universe to an unprecedented accuracy. In the era of advancing new generation IR facilities like James Webb Space Telescope (JWST) and WFIRST, our estimates provide a critical reference for all galaxy formation models.

Advancement of the new surveys like DES, Pan-STARRS, HSC, KiDS, DECaLS and VIKING opens a new era of deep panoramic multiband imaging with areas over thousands of square degrees. Data from these surveys shall be used in a numer-

ous ways - from obtaining cosmological constraints to galaxy evolution and number density of objects in the early Universe, from measuring the growth of galaxies to observing the transition between different populations of galaxies at different epochs. Advance of the Big Data in astronomy requires new efficient approach in combining large data sets from different telescopes and different bands in a consistent, robust way. In this project we used various software codes to process thousands of images and terabytes of data using computational clusters. Algorithms that were developed for the purpose of this dissertation will be used in the follow-up projects.

As a by-product, we also compile a large sample of optical-dropouts, which are objects detected in the near-IR by WISE but are missing from the SDSS in optical. The nature of these extremely red objects (ERO), [Graham and Dey, 1996], [Yan et al., 2004] is not well understood, and this unique sample will provide an important input catalog for future studies at the next generation telescopes, including JWST.

The structure of this thesis is as follows: In Chapter 2 we present the data sets that we use in our study and also some preliminary operations with images that ought to be done in order to construct sources catalogs. Construction of such catalogs and problems associated with it are discussed in Chapter 3. SED fitting that allows us to derive physical properties of the galaxies is presented in Chapter 4. We use Chapter 5 to discuss our final results - evolution of stellar mass density over last 6 Gyr and compare our results to other groups. Chapter 6 concludes our work, we put our results in the context of the study of the galaxy evolution, describe future work, including a study on a separate population of objects that we call "WoDrops".

Throughout the thesis we use a $H_0 = 70 \text{ km s}^{-1} \text{ Mpc}^{-1}$, $\Omega_\Lambda = 0.7$ and $\Omega_m = 0.3$ cosmology, and assume that the distribution of the stellar mass follows [Bielby et al.,

[2012] initial mass function (IMF). Such IMF gives stellar masses consistent with [Kroupa, 2001] IMF to within 10% and are different from [Salpeter, 1955] IMF by a constant factor 1.64.

Chapter 2

Data

SED fitting is now a standard technique of deriving stellar mass for a large set of galaxies. In this method multi-band photometry for a given galaxy is fitted to a series of templates predicted by a certain population synthesis model. The best-fit template gives the parameters of the galaxy, including its redshift and mass. Historically, population synthesis models were using restframe optical photometry. One caveat is the degeneracy between the dust extinction and age of the stellar population, as both make the color of galaxy red, i.e. galaxy can be red because it is intrinsically red with no star formation, or it can be very dusty, or there could be lots of metals that effectively absorb light in the bluer bands. Solution to this is to implement restframe near-IR where light suffers much less extinction (comparing to restframe UV and optical) and thus the degeneracy can be broken. We aim to build the largest sample of galaxies with optical and near-IR photometry over a large sky area. The natural choice for us then is to use optical Sloan Digital Sky Survey (SDSS) and IR all-sky data from Wide-Field Infrared Survey Explorer (WISE).

2.1 SDSS

SDSS [York et al., 2000] was an imaging and spectroscopic survey with a dedicated 2.5m telescope at Apache Point Observatory. Imaging is performed by 142 mega-pixel camera as shown on Figure 2.1, that uses the drift-scan mode in five broad optical filters, namely *ugriz* [Gunn et al., 1998] spanning from 3,000 to 10,000 Å. While the spectroscopic survey is still carried on, the imaging survey has been completed and by now their data covers $14,555 \text{ deg}^2$ of unique sky area with pixel scale $0.396''$. Exposure time is 53.9 seconds per band. An SDSS run consists of six parallel scanlines. The skylines are $13.5'$ wide with the gaps between them of relatively same size. Two interleaving runs make stripe that consists of total 12 scanlines (columns).

2.1.1 Stripe 82

Single-pass images are shallow (magnitude limit in r-band is 22.2 AB) and is not suitable for our purposes. For that reason we shall use Stripe 82, a ≈ 300 sq.degree area on the Celestial Equator in the South Galactic Cap in the Fall [Adelman-McCarthy and et al., 2007]. Stripe 82 is a deep survey stripe that spans $20h < RA < 4h$ and $-1.26 < Dec < 1.26$. This area was repeatedly used for calibration purposes and was scanned 70-90 times depending on RA. The advantage of these multiepoch images was quickly anticipated by various teams who stacked it and created co-added images. Annis et al. [Annis et al., 2014] produced the first version of stacked images. They combined images available by December, 2005 (20-35 runs) and achieved magnitude limit 1-2 mag deeper then single-epoch SDSS products. results were published in SDSS Data Release 7 (DR7). Several teams produced their own co-adds using different strategy for the selection and post-processing of images (e.g. Huff et al. 2014 [Huff et al., 2014], Jiang et al. 2009 [Jiang et al., 2009]). It is important to outline that images were taken under different photometric conditions (e.g. significant moonlight

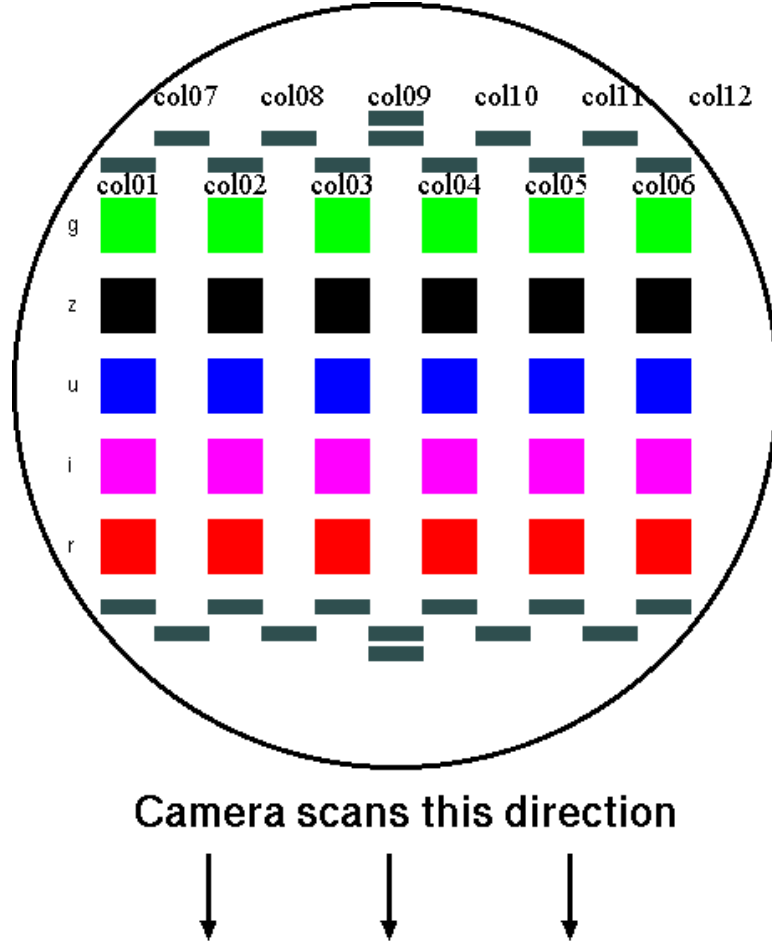


Figure 2.1: The camera used for imaging. It consists of 30 photometric CCDs, that are arranged in 6 columns of 5 each. Camera is drifted in the way that each column has permanent Declination during the run and all 5 filters in a column consequently go over the same field

and poor seeing in several runs performed in 2005-2007) and thus certain selection of the images has to be performed.

Jiang et al. 2014 (J14) [[Jiang et al., 2014](#)] released a new version of co-adds in which only images that had been taken under perfect photometric conditions were used. These co-adds, that we shall use in our work are in general 0.2 mag deeper than in Annis et al. and 2 mag deeper than single-epoch SDSS images (see fig 7 in J14) and reach detection limit of 23.9, 25.1, 24.6, 24.1, and 22.8 AB magnitudes in bands u-, g-, r-, i- and z- respectively at 5σ .

2.1.2 Structure of SDSS Stripe 82 files

We use description from J14 to present the structure of optical data. An SDSS run (strip) consists of six parallel scanlines, identified by camera columns (Figure 2.1). The scanlines are 13.5 arcmin wide, with gaps of roughly the same width, so two interleaving strips make a stripe. That creates the following sequence of columns in the direction of increasing declination: $col01 \rightarrow col07 \rightarrow col02 \rightarrow col08 \rightarrow col03 \rightarrow col09 \rightarrow col04 \rightarrow col10 \rightarrow col05 \rightarrow col11 \rightarrow col06 \rightarrow col12$.

The size of each SDSS image is 1489 x 2048 pixels, or roughly 9.8 x 13.5 arcmin (RA x Dec), with a pixel size of 0.396 "/pix and an average full width at half maximum (FWHM) of $\sim 1.5''$ in u-band, $\sim 1.3''$ in g-band, and $\sim 1''$ in r-, i-, and z-bands. In total there are 401 SDSS images in each column and there are total $12 \cdot 401 \cdot 5 = 24,060$ SDSS images. Between any two adjacent images there is an overlap region with a width of 128 pixels along the scan direction. Catalogs that we produce will have duplicate sources for such regions and it shall be removed in the post-processing stage by internal matching of all sources in the final catalog using the matching radius of 1.2''. This radius was determined empirically to be the largest at which we do not have false rejections - rejection of two sources that lay very close to each other on the line of sight. Images are named by their band, column and sequential number, e.g. *S82_11x_222.fits*, where 11 is the column number, x - letter for one of the five bands, and 222 - sequential number. Each SDSS image has a corresponding weight.fits image, that records relative weights at individual pixels.

2.2 WISE

WISE [Wright et al., 2010] was a near-IR space observatory that was launched in 2009 and mapped the entire sky with sensitivity far better than that of its predecessors, IRAS [Neugebauer et al., 1984] and DIRBE [Silverberg et al., 1993]. With a 0.4

m telescope on board always pointing at 90 degrees solar elongation, WISE made successful scans of the entire sky in four bands, namely w1 ($3.4\mu m$), w2 ($4.6\mu m$), w3 ($12\mu m$) and w4 ($22\mu m$). Its observations have very wide range of applications from search of near-Earth asteroids and brown dwarfs to the studies of the most luminous galaxies in the Universe.

2.2.1 unWISE

WISE data are published as a set of co-added data. Stacks were created by the WISE/NEOWISE team using the first 13 months of data (the AllWISE release) and are available at NASA/IPAC [Infrared Science Archive](#)¹. Original images were intentionally blurred by the WISE point spread function (PSF) for better detection of deep single sources. But that leads to the blending problem in the crowded fields and also decreases the signal-to-noise ratio (SNR) due to the broadening the of the PSF. D.Lang [[Lang, 2014](#)] has produced custom unWISE stacks analogous to the AllWISE images, but at the full spatial resolution of the instrument - $2.75''/\text{pixel}$.

2.2.2 Structure of unWISE files

Structure and naming convention of unWISE files is taken from [unwise.me](#)². The unWISE coadds are on the same tile centers as the WISE Images: 18,240 tiles per band, 1.56×1.56 degrees each. The tiles are named by their RA, Dec center: tile "0591p530" is at RA = 59.1, Dec = +53.0 degrees; i.e., the first four digits of the tile name is $\text{int}(RA \cdot 10)$, then "p" for +Dec and "m" for -Dec, then three digits of $\text{int}(\text{abs}(Dec) * 10)$. For each tile and band w1-w4, several images are produced, we shall list only the ones that we make use of:

- unwise-0000p000-w1-img-m.fits - "Masked" image, 2048 x 2048 pixels, TAN

¹<http://irsa.ipac.caltech.edu>

²<http://unwise.me/data>

projected at $2.75''/\text{pixel}$. Background-subtracted, in units of "Vega nanomaggies" per pixel: $\text{mag} = -2.5 \cdot (\log_{10}(\text{flux}) - 9)$. This is our science image. The word "masked" means that some pixels will have no unmasked pixels and no measurement at all: pixel value 0 and infinite uncertainty.

- unwise-0000p000-w1-std-m.fits - Sample standard deviation (scatter) of the individual-exposure pixels contributing to this coadd pixel. This will be large if, for example, the source is variable.

One unWISE FITS image may cover up to 72 SDSS images within its footprint. We shall call one unWISE image or a set of SDSS images within this area "a frame".

In each band there are 240 unWISE frames that fall within Stripe 82 footprint that create 3 sets of frames in declination, 80 frames per set: centered at Dec=-1.6, Dec=0.0 and Dec=+1.5 degrees. Two adjacent frames overlap by $\sim 174''$ and sources that appear in such regions will be duplicated. Such sources, as in the case of the overlapping SDSS images, shall be removed in the post-processing stage.

Chapter 3

Construction of the multiband catalog over Stripe 82

SED fitting requires supplying catalogs that contains multi-wavelength photometry. Quality of photometric data is very important for proper estimate of the properties of the galaxies. In this chapter we shall describe our strategy for construction of such catalogs, optical and IR, general issues that arise and our methods to solve it.

- SDSS co-adds from J14 that we utilize already have catalogs associated with them
- they run **SExtractor** on the whole Stripe 82 region. We decide not to use it and create our own catalogs for several reasons:
 - The catalogs are not matched between the bands, resulting in different object lists for each band within the same region, thus if there may be misidentification of the sources when we attempt to construct multiband catalog with data from all 5 bands.
 - SNR at which the source is rejected from the catalog was chosen too high and there are a lot of sources that we shall use, but that are not included in J14 catalog.
 - Bright and saturated objects are generally represented in the catalogs as a set of sources, none of which is at the center of such object. This means that if such source is supplied to **TPHOT**, we shall get a non-physical photometry and eventually non-

physical stellar mass that will significantly bias our results.

On Figure 3.1 we present a comparison of the original catalog from J14 (sources within green regions) and our catalog, that was constructed independently (sources within red regions) and will be presented further in this chapter.

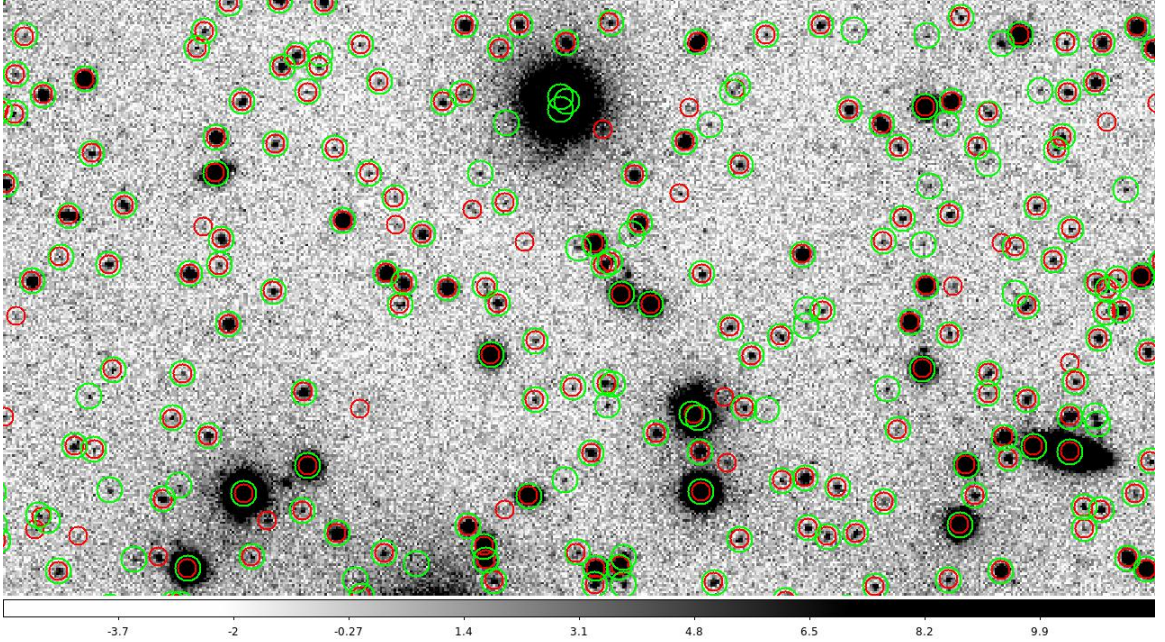


Figure 3.1: Optical catalogs from J14 (denoted with green circles) and our catalog (red circles) are overplotted on a small random area in Stripe 82. There is a number of well-detected sources that were excluded from J14 catalog and also there are multiple detections around a saturated source in the upper part of the plot. Our catalog aims to resolve both such issues.

The most critical factor in the success of this project is consistent photometry from optical to near-IR. This is challenging because the spatial resolutions of WISE is $\sim 5\text{-}6$ x worse than that of SDSS. For this reason, the objects detected in WISE often suffer blending. Even for relatively isolated WISE sources, the photometric apertures appropriate for the (low resolution) WISE images cannot guarantee the same fraction of light being included as what is done in the (high resolution) SDSS images. Such a systematic offset, which is different for every galaxy of different morphology, can severely skew the SED fitting.

To best address this problem, we opt to use the TPHOT software [Merlin et al., 12]

2016], which recently emerged as a robust and flexible tool to perform "template fitting". The basic idea is to use a high-resolution image (here SDSS) as the prior to build the morphological template of the source under question, convolve this template with the PSF of the low-resolution image (here WISE), and fit this degraded template to the low-resolution image to obtain the total flux that is within the aperture as defined by the high-resolution image. In this way, we get reliable color information (i.e., flux ratio) in the most consistent manner. It is important to note that high-resolution source does not have to be point-like - its morphological features will be preserved and fitted to the low-resolution source. This implies the biggest assumption for this technique - that morphology of the source is wavelength-independent. While generally it is not always true, especially for the actively star-forming or dusty galaxies, we anticipate that this will not create any significant bias. Firstly, because most of the galaxies have small angular sizes and such variation in sizes is small, and secondly, because we chose SDSS r-band (6202.46 \AA), that is a red filter, as a high-resolution image.

Proper use of TPHOT requires several preliminary operations with both high- and low-resolution images, and construction of optical catalogs also consists of a number of steps. It is impossible to separate operations for these two main stages - chronologically the steps for both stages are intermixed. In the following sections we shall describe general algorithm in the order in which it was implemented in the project.

3.1 Preparatory work with SDSS images and optical catalog

High-resolution optical image is used not only to determine flux and morphology of the source in near-IR, but also its position. For that reason high- and low-resolution

images should have the same type of projection, reference coordinate and orientation written in their FITS headers [Pence et al., 2010]. SDSS and WISE images have the same tangential projection and orientation ($CD1_2 = 0$, $CD2_1 = 0$), so we leave these values unchanged. Each WISE frame covers $\approx 3.95\text{deg}^2$ and there may be up to 72 SDSS images that cover the same area, so we decide to use coordinates of the center of WISE images (CRVAL1 and CRVAL2) as the anchor values and run **SWarp** [Bertin et al., 2002] to change reference pixels in all SDSS images. The reference pixel (CRPIX1 and CRPIX2) for SDSS images can now be outside of the image itself to as far as 0.7 deg.

3.1.1 Region of overlapping unWISE images

Some SDSS images may reside on the border between two overlapping unWISE images. In such a case 2 copies of SDSS image are created and each is processed by **SWarp** independently, gets its own set of CRPIX and CRVAL values and from now on is treated separately. The following example shows the current naming convention that will be used throughout this work: *S82_3282m016_01r_097.fits* and *S82_3297m016_01r_097.fits* means that original image *S82_01r_097.fits* now has two sets of CRVAL values - one is the same as the coordinates of the center of image *unwise-3282m016-w1-img-m.fits* and the other - of image *unwise-3297m016-w1-img-m.fits*.

This "duplication" increased the number of SDSS images in each band from 4,812 to 5,556.

3.1.2 SDSS PSF construction

Optical part of the catalog consists of 5 SDSS bands, each of which has different sensitivity and FWHM, so each field has different number of sources in different

bands. We shall choose the band that we use for detection, i.e., the source is added to our catalog if only it is detected in this band with sufficient SNR. Also position of the source in this band is used as its true position in all other bands. Another issue is the flux measurement - reliable SED fitting requires consistent multiwavelength photometry while different photometric conditions and FWHM could result in a non-consistent colors even in optical filters alone. Thus the measurement that are made even with flexible elliptical apertures known as the Kron apertures [Kron, 1980] that are denoted in `SExtractor` as `FLUX_AUTO` [Bertin and Arnouts, 1996] will not be measuring the same fraction of the total flux from the given source in different filters. We decided to convolve *griz* bands to the one with the worst FWHM, i.e., u-band. In such case the difference in sizes will be due to the intrinsic difference in morphology at different wavelength rather than due to difference in optics. For the price of loosing some sources due to blending we shall achieve better consistency in our optical colors. We use `IRAF/psfmatch` task that requires supplying the image with the corresponding kernel - PSF matching function to be convolved with the input image to produce the output one. Construction of a kernel requires a knowledge of the PSFs of the input image and a matched image. We need to construct PSF for each image in each band ($5, 556 \cdot 5 = 27,780$ PSFs) and this is the most time-consuming part of the project.

One of the widely-used ways to construct a PSF is using `PSFEx` software [Bertin, 2011]. We tested it with `TPHOT` and found that the quality of residual images is not satisfactory, so we decided to use more conservative algorithm in which `IRAF/psf` task creates a PSF function based on a set of selected point-like sources (so called PSF stars). Usually that strategy involves consecutive run of `IRAF/find`, `IRAF/phot`, `IRAF/pstselect` and `IRAF/psf` tasks that find stars, determine its magnitude, select the ones that do not have any morphological features and finally construct a PSF function. This algorithm is not ideal - in each image there are $\sim 10\%$ of sources that do not satisfy the criteria of PSF stars (are elongated, blended or have noisy

background) and have to be rejected in the manual regime (selection in interactive mode). This is extremely time-consuming and inefficient given the total number of images in 5 bands. We decide to use a variation of this method to create PSF functions in a more automatic fashion.

We run **SExtractor** on each SDSS image and only mark a sources from the output catalog as a point-like, if their "stellarity" index (determined by a CLASS_STAR parameter) is close to 1, sources are bright, but not saturated, do not lay within $2 \cdot PSF\ radius$ to the edge of the FITS image, and have all their flux contained within some small aperture. The later was confirmed by comparing MAG_APER that returns all flux within some fixed aperture and MAG_BEST that returns MAG_AUTO value in the absence of contamination from the nearby sources and MAG_ISOCOR otherwise. Exact parameters depend on the band and also were adjusted during test runs so that each SDSS image has no less than 20 PSF stars (stars were sorted by their magnitude, from bright to dim), with the maximum number of PSF stars limited to 160 (larger values slow down **IRAF** and could even crash the task). Selection criteria can be found in Table 3.1

Table 3.1: Table of parameters for selection of PSF stars

parameter	u	g	r	i	z
MAG_APER - MAG_BEST	-0.06 – -0.14	-0.04 – -0.1	-0.1 – 0.7	-0.1 – 0.7	-0.1 – 0.7
CLASS_STAR min	0.80	0.85	0.85	0.85	0.80
MAG_AUTO min	13.5	13.8	14.2	13.7	13.1
MAG_AUTO max	19.0	19.3	19.2	19.1	19.0

Selected PSF stars were supplied to **IRAF/psf** to create PSF files. This task was run in a non-interactive (automatic) mode with parameters listed in Table 3.2

Parameters that were the same for all bands:

```
functio= moffat25
```

```
matchra= 3
```

Table 3.2: Table of parameters for **IRAF/psf** task.

parameter	u	g	r	i	z
fitrad	2.9	2.8	2.7	2.7	2.8
fwhm _{psf}	2.9	2.8	2.65	2.65	2.8
sigma	0.48	0.70	0.65	0.48	0.77

```
psfrad = 12
nclean = 3
noise = poisson
```

After we obtain all PSF functions for our sample, we run **IRAF/seepsf**, a task that takes the input PSF computed by the **IRAF/psf** task, consisting of the parameters of a 2D analytic function stored in the image header, and computes 21x21 pixel output PSF FITS image consisting of the sum of the analytic function and the residuals. Visual inspection of all PSF images reveals a certain fraction of defect PSFs. The reason it can be either a blended source within the PSF radius, high background values due to the nearby bright star (within up to several arcmin), or noticeable elongation of the source (may be due to inclusion of a galaxy in our sample or due to intrinsic problems with SDSS image).

The fraction of such images varied in different bands but generally was $\sim 4\%$ and for such images we re-run **IRAF/psf** in interactive mode (manually selecting PSF stars from a catalog). All PSF images were scaled to unit flux using **wcstools/sumpix** [Mink, 1998] and **IRAF/imarith** tasks. Several PSFs for all 5 bands and 6 different columns centered at RA=21:56:46 are shown in Figure 3.2

We used **IRAF/lucy**, a task that uses algorithm developed independently by Lucy [Lucy, 1974] and Richardson [Richardson, 1972], to create kernels for pairs of images in x- and u-bands, where "x-" stands for g-, r-, i-, or z-band. Parameters for **IRAF/lucy** :

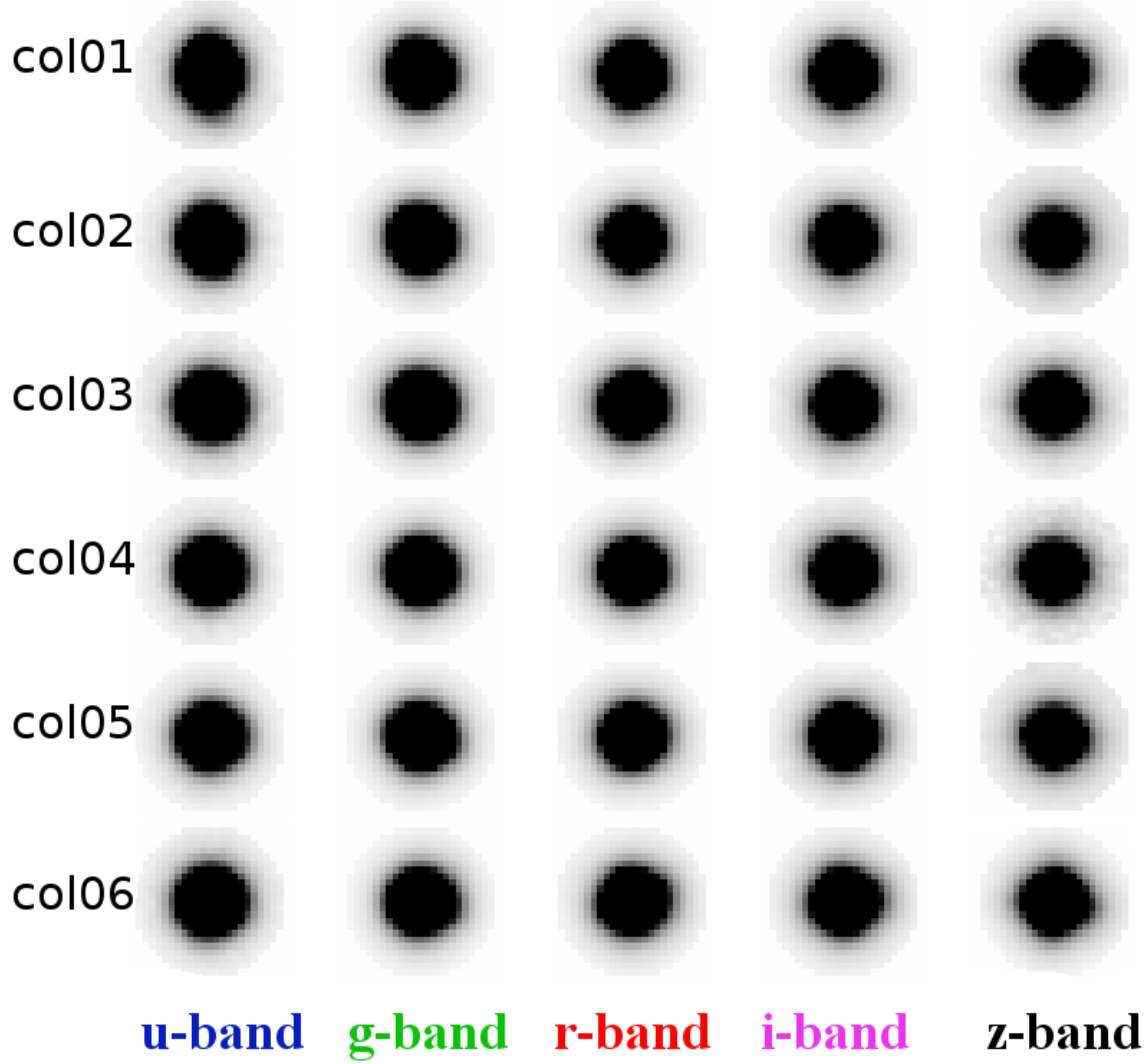


Figure 3.2: A set of PSFs for five bands for odd columns centered at RA=21:56:46. All PSFs are scaled to the unit flux

```
input = u-band PSF
psf = g-, r-, i-, or z-band PSF
niter = 50
limchis= 1.0E - 14
accel_m= standard
```

With kernels in hand it is now possible to run `IRAF/psfmatch` that convolves input image with the kernel to produce a psf matched output image (Figure 3.3).

Parameters for IRAF/psfmatch :

```
input = g-, r-, i-, or z-band FITS file  
kernel = kernel.fits  
output = x_matched_u.fits  
convolu = kernel
```

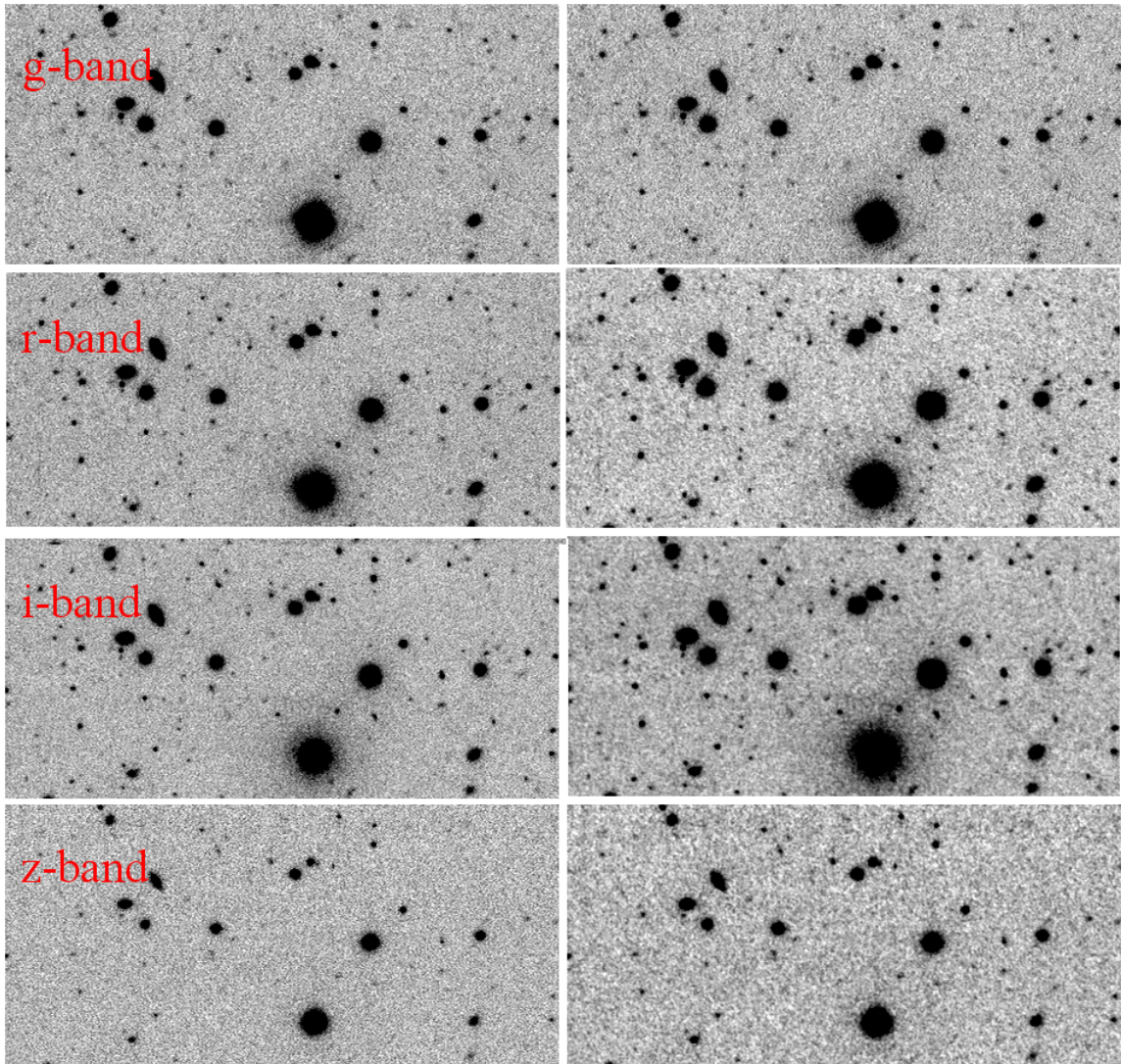


Figure 3.3: An example of IRAF/psfmatch for *griz* bands (top to bottom). Original images are to the left, PSF-matched - to the right. The difference is mostly observable for r- and i-bands, because their PSF is much better than that in u-band

3.1.3 Construction of the optical part of the catalog

As outlined above, different bands have different sensitivity and FWHM, so faint sources may not be detected in all bands. In order to construct our catalogs we ought to select one band as the detection band. It has to be deep enough to have as many sources as possible and also has good FWHM to constrain the shape of the sources - that is crucial for the flux measurement in unWISE bands as each image must be supplied to TPHOT along with the corresponding segmentation file and also each source in the catalog must have its `x_min`, `x_max`, `y_min` and `y_max` values. As can be seen on Fig.9 from J14, *riz* bands have the best FWHM out of 5 bands, but r-band has the highest limiting magnitude out of these bands (24.6, comparing to 24.1 and 22.8 AB magnitudes in i- and z-band respectively). We choose r-band to be the base catalog of our sample and we used position of the source in this band to extract flux in *ugiz* bands in SDSS and also in w1 and w2 bands of unWISE images.

Now we run `SExtractor` in the dual mode (the first image is used for detection and astrometry information, while the second is used solely for photometry) to create a 5-band optical catalog. We use `r_matched_u` images for the detection of sources and `x_matched_u` image for the photometry, (`u_matched_u` is just u-band image). All bands are PSF matched to the u-band, so `SExtractor` parameters are identical. Complete list of parameters is provided in [Appendix](#). As the next step we reject sources with $\text{SNR} < 5$ based on the `r_matched_u` flux. We noticed that very few sources were rejected at this stage. Objects that appear almost undetectable had `FLUX_AUTO / FLUXERR_AUTO` larger than 5 or even 7. We address this issue in the next section, and note that we decide not to reject those sources and supply it to TPHOT because we shall use residual images to detect "WoDrops" - objects that are undetectable in optical bands. i.e., dropouts. But for the purpose of the GSMD construction we rejected sources with $\text{SNR} < 5$ before starting the SED fitting.

3.1.4 Magnitude error correction

Photometry comparison between original x-band and x_matched_u-band catalogs shows a systematic underestimation of the errors associated with the sources' flux (Figure 3.4). To correct for that we use **STILTS** code [Taylor, 2006] to match x-band and x_matched_u catalogs in 5 bands and for each separate image we calculate the mean ratio of the flux error before and after PSF. All magnitude errors in a given image are then multiplied by this coefficient. This correction coefficient can also be used as a test of our PSFs - coefficients should occupy a narrow region with values within 1.2-2.2 for *griz* bands with very few outliers (Figure 3.5). We did not apply **IRAF/psfmatch** task to the u-band, but still calculated that correcting coefficient because r_matched_u FITS file was used as detection image in **SExtractor**. All coefficients for this band are less than 1.

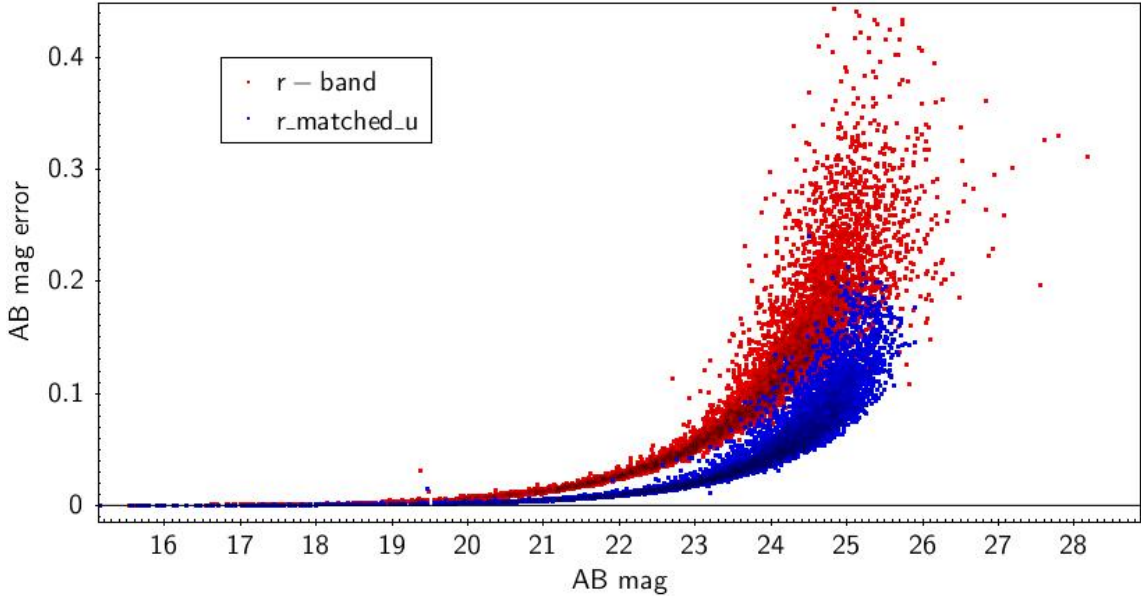


Figure 3.4: An example of the change in magnitude error for r-band photometry. Original errors are plotted against AB mag in red, magnitude errors *for the same source* after **IRAF/psfmatch** is performed are in blue.

We anticipate that while corrected values account for statistical error, there should also be a systematic error in magnitude that needs to be taken care of. We performed

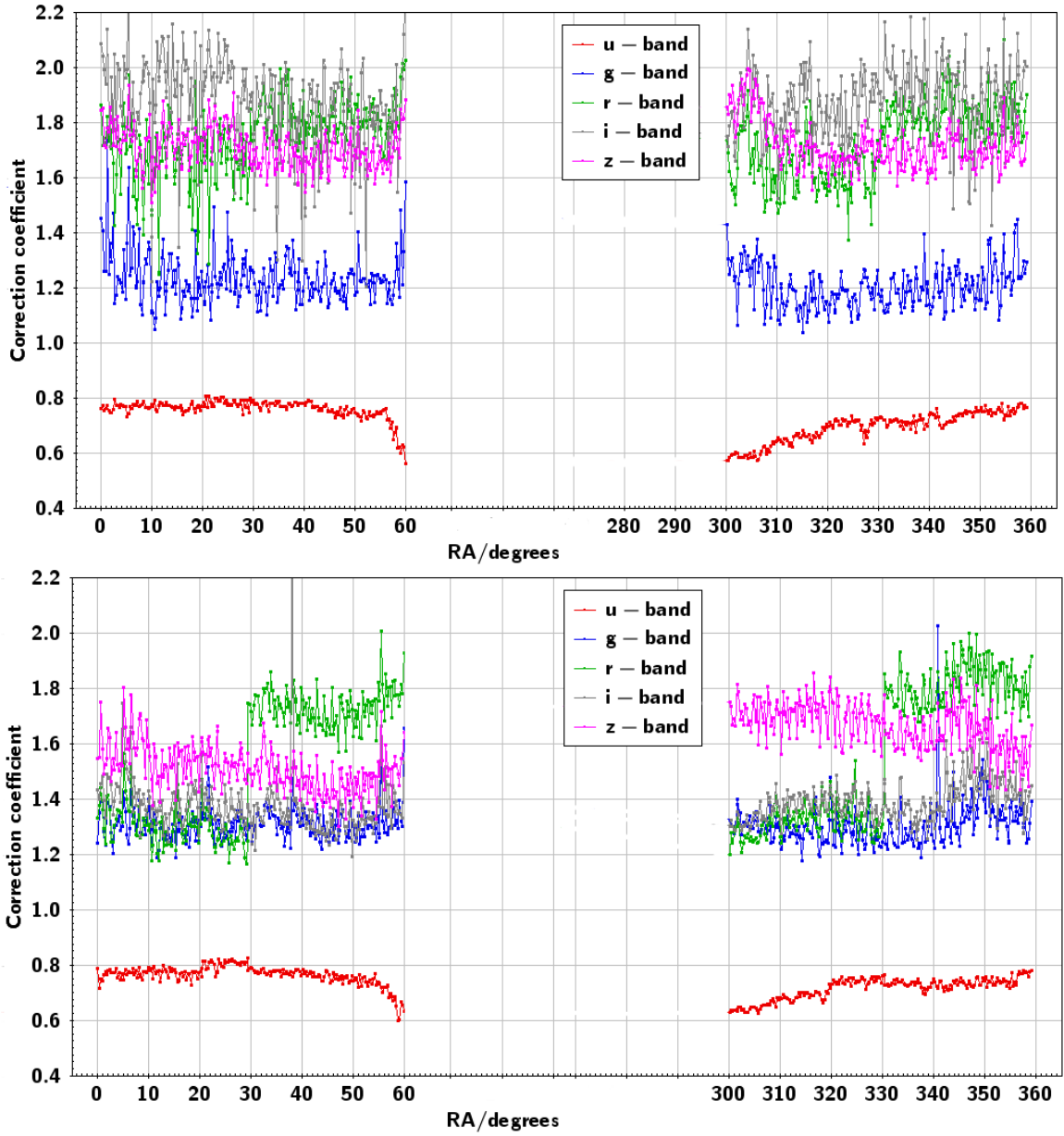


Figure 3.5: Correction coefficients for all 5 bands for two columns - col04 (top) and col12 (bottom). Note that coefficients for the u-band are less than one

a series of tests where different constant errors were added in quadrature to the reported magnitude error and then the goodness of fit on the graph z_{spec} vs z_{phot} was checked. We found that the tightest correlation is achieved when 0.04 magnitude error is added in quadrature (so final error cannot be smaller than 0.04). Each source in each band was assigned by a error in magnitude that was calculated using the

following equation:

$$magerr_corrected = \sqrt{0.04^2 + \left(\frac{1.0857}{SNR} \cdot correction_coefficient\right)^2}$$

At this point construction of the optical part of the sample is complete. Our parent catalog now consists of 26,585,000 sources.

3.2 Preparatory work with unWISE files

TPHOT is very demanding to the quality of the input files, any small variation severely skews results, so we pay particular attention to this part.

3.2.1 unWISE PSF construction

We use **SWarp** to change the pixel scale of all unWISE images from original 2.75 to 2.772 to match the integer pixel scale ratio with SDSS images $\frac{2.772}{0.396} = 7$. Now we construct unWISE PSF functions that will be convolved with SDSS PSF to create kernels - one of the most important input files to TPHOT. There are 240 unWISE images within Stripe 82 footprint for each IR band. Bands w3 and w4 are much more shallow and no reasonable flux can be extracted for the vast majority of optical sources in these bands, so for the purpose of this project we only use w1 and w2 bands. That means we need to make another 480 PSFs. We followed the strategy from the previous section to construct PSF for all 480 images (i.e., running **SExtractor**, selecting potential PSF stars using **STILTS**) with two major differences in the procedure:

- 1) Center pixels of saturated sources in unWISE standard deviation images (`unwise-0000p000-w1-std-m.fits`) always have zero value and that is an invalid input for TPHOT. We use **IRAF/imcalc** to detect such pixels and change its value to "9999".
- 2) We construct each PSF function manually, using **IRAF/psf** in interactive mode.

This was done to perform more robust selection of stars as 3 PSFs from one unWISE frame are convolved with up to 72 SDSS PSFs and thus its quality is crucial because incorrect PSF profile will lead to characteristic positive and negative ring-shaped patterns in the residuals.

After running the `IRAF/seepsf` task we got PSF FITS images, 19x19 pixels each. All unWISE PSFs were scaled to the unit flux with `IRAF/imarith` and sub-sampled in size by the factor of 7 using `IRAF/imlintran` (to 133x133 pixels) to match the pixel scale ratio of the unWISE and SDSS images. Result is presented on Figure 3.6

3.2.2 Naming convention for the processed files

Both final and intermediate results are a combination of SDSS and unWISE data and we introduce our naming convention that is used throughout the project. E.g. file `kernel.w1.0000p015_12r_u_111.fits` is a kernel made by convolution of the PSF function of the file `unwise-0000p015-w1-img-m.fits` and PSF function of the file `S82_12r_111.fits` in r-band, that has been previously matched to the PSF of the u-band.

3.3 Template fitting with TPHOT

TPHOT is a software designed to perform a precision photometry on a low-resolution images using information provided by a high-resolution images of the same field. Running TPHOT on such a large portion of the sky with individual kernels for every pair of high- and low-resolution image is a key feature of our project.

In order to get the best results we follow recommendations of E.Merlin and perform two runs ("pass 1" and "pass 2") of TPHOT on each pair (low- and high-resolution) of images. The second pass is performed using local kernels registered after the shifts in x and y coordinates are determined in the first pass.

One of the advantaged of TPHOT is a large saving of computational time comparing

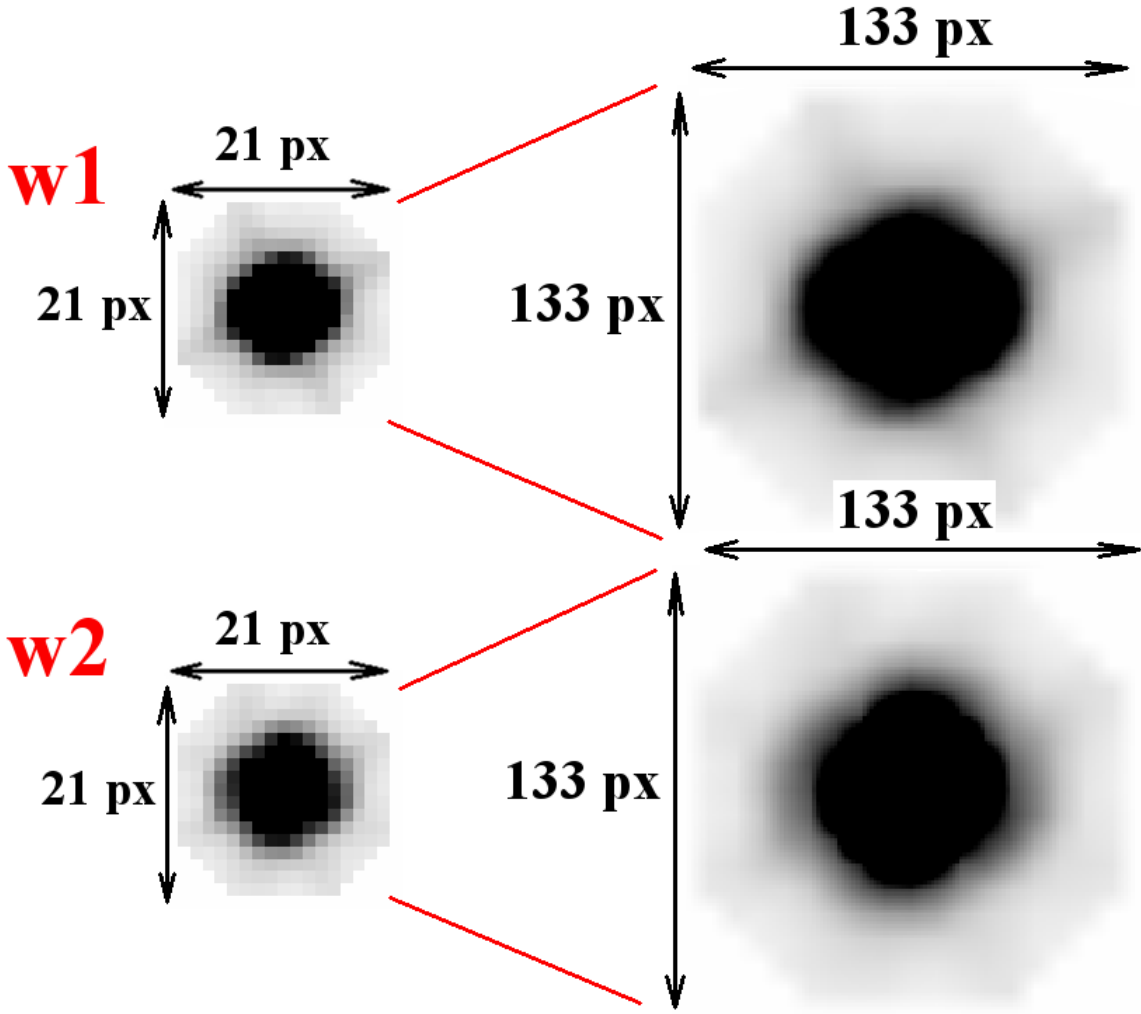


Figure 3.6: unWISE PSFs for w1 (top row) and w2 bands (bottom row), as constructed in `IRAF/psf` (left) and scaled by factor x7 to mimic pixel scale ration between SDSS and unWISE pixel scales (right)

to its forerunners, `TFIT` or `CONVPHOT` codes, but it still needs lots of CPU time. Each SDSS image has on average 5200 sources and each pass of `TPHOT` takes ~ 3 hours CPU time. We perform template fitting on two unWISE bands so the total number of passes is $5556 \cdot 2 \cdot 2$ that requires $\approx 66,700$ CPU hours. We use our access to the University of Missouri High-Performance Computing (HPC) cluster Lewis to process all images.

There are six different files supplied as an input to each run of `TPHOT`:

- High-resolution image - SDSS r-band FITS image matched to the u-band PSF
- Source catalog with position, flux and background measurements for each source
- Segmentation map corresponding to the SDSS image and having the value of the id of each source in the pixels belonging to it, and zero everywhere else
- Low-resolution image - unWISE either w1 or w2 FITS image
- Low-resolution weight image
- kernel - result of convolution of high- and low-resolution PSFs

Dimensions of high- and low-resolution images do not have to be the same for successful run of TPHOT, so generally we can supply full unWISE frame as the low-resolution image, but the code performs certain mathematical operations on such image during each pass, and such operations are mutually interfering when one tries to simultaneously run TPHOT on several SDSS images that belong to the same unWISE frame. In order to run several TPHOT jobs at the same time at Lewis cluster we created 18.828'x13.523' unWISE cutouts (with associated weight image) for each SDSS image.

After considerable number of test runs we came up to the following set of parameters that provides us with the best results. We only list the most important parameters here, full list is available in [Appendix](#):

```
order standard # Used for the first pass
order standard2 # Used for the second pass
usereal True # Real 2-d profiles
relscale 7 # Pixel ratio between detection and measure image
FFTconv true # Use FFT for convolution of cutouts
fitting single # One of three possible fitting methods
fitbackground false
clip true # Clip out large negative fluxes and re-do the fit
dzonesize 5 # Pixels size of region in which PSF shift is computed
```

3.3.1 TPHOT output files

The most important TPHOT output files are low-resolution residual FITS image, which is obtained by subtracting the model image from the low-resolution image, and catalog of residual fluxes and corresponding flux errors for each input source that was successfully fitted. TPHOT rejects source if it lies outside of the low-resolution frame or if it has too high RMS. For such rejected source the fitted flux and flux errors is assigned to be -99 and $99.0E8$ respectively - such source is still used for SED fitting and we do not create any special subsample for the sources without near-IR photometry). On Figure 3.7 three images are shown - r-band SDSS, w1-band unWISE and residual in w1-band. Red circles with $3''$ radius are drawn around optical sources that are supplied to TPHOT.

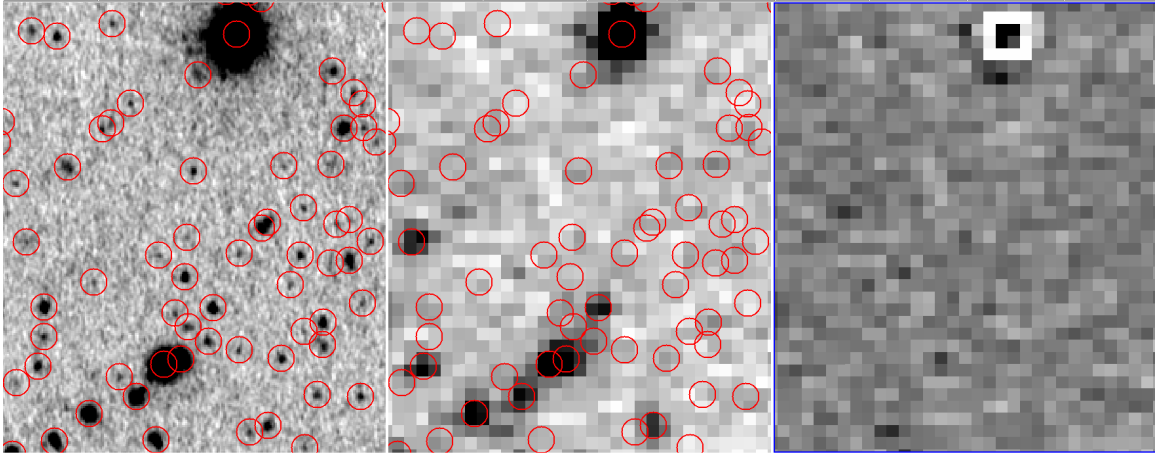


Figure 3.7: From left to right: SDSS image in r-band, unWISE w1 image, residual image from TPHOT. SDSS sources that are fitted to the unWISE image for the flux estimation are denoted with red circles. These objects are cleaned out from the residual image

3.4 Matching optical and IR catalogs

Once all unWISE images within Stripe 82 footprint in w1 and w2 bands are processed by TPHOT, output catalogs need to be matched with optical ones. Matching is performed with STILTS code by using the source ID as the parameter to match. Additional test is performed in order to verify that photometry in optical and IR indeed belongs to the same source: difference in r-band FLUX_ISO and TPHOT input flux in both bands is calculated and it should be zero.

As the next step fluxes in the matched catalogs are converted from counts/sec to AB magnitudes and flux in microJansky.

Chapter 4

Mass and redshift estimation

Fitting the spectral energy distributions (SEDs) of galaxies is an almost universally used technique to derive a range of physical properties of galaxies, such as redshift, stellar masses, star formation rates, dust masses, and metallicities (though there is a temptation to over-interpret the available data, so results should be taken with caution). SED fitting has matured significantly in the last decade and model predictions and fitting procedures have increased the precision of the results, attempting to keep up with the vastly increased volume and quality of available data. For this project we will use SED fitting to estimate redshift of individual galaxies and their corresponding stellar mass.

Traditionally, photometric redshift estimation is generally presented by two large groups of algorithms: empirical methods and the template-fitting methods. Empirical methods use a subsample of the photometric survey with spectroscopically-measured redshifts as a "training set" for the redshift estimators. This subsample describes the redshift distribution in magnitude and color space empirically and is used then for calibration of the whole sample. We list several codes training set based codes: ANNz [Collister and Lahav, 2004], RFPhotoZ [Carliles et al., 2008], Singal [Singal et al., 2011]. Template methods use libraries of either observed spectra of galaxies exterior

to the survey or template SEDs, that are built using different stellar population synthesis (SPS) models. As these spectra are produced artificially, they span over full spectra, and templates can be shifted to any redshift and then convolved with the transmission curves of the filters used in the photometric survey to create the template set for the redshift estimators. Among the some widely used template based codes we list BPZ [Benítez, 2011], HYPERZ [Bolzonella et al., 2011] and Kcorrect [Blanton and Roweis, 2017]. Both methods then use these training sets as bases for the redshift estimating routines, which include χ^2 -fitting and various machine learning algorithms (e.g. artificial neural networks, ANNs). A good review of the present the state of the art in the area of fitting SED of galaxies is presented in [Walcher et al., 2011] and a list of codes with documentation, reviews, discussions and templates is available at [sedfitting.org](http://www.sedfitting.org)¹

For several years best results in SED fitting were obtained by the codes that calculate redshift based on the flux determined from the red-sequence stars - redMaPPer [Rykoff et al., 2014], redMaGiC [Rozo et al., 2015] or that use a trained neural network (ANNz [Collister and Lahav, 2004]). Recent studies [Bundy et al., 2015] show that these codes get twice smaller scatter of photo_z vs spec_z for massive galaxies. But for the faint galaxies (i-band magnitude > 22.5 AB), template codes perform slightly better, probably because of the smaller training sets available for neural networks and obviously poorer photometry. Our catalog consists of over 23 millions of objects, and calculation speed is an important factor for the section of the fitting code. Computationally, most template-fitting codes benchmark roughly similarly, while the training codes are much faster to evaluate the redshifts but only after their training is complete. The quality of our data was refining while the project was already ongoing and we did not attempt to use the empirical-based codes as it would have required re-computation of the training set after each change in the algorithm (e.g., we did

¹<http://www.sedfitting.org/Fitting.html>

not plan to perform matching to the u-band PSF originally).

4.1 SED fitting

4.1.1 Choice of SED fitting codes

A special case of analyzing SEDs of extragalactic sources is the problem of redshift estimation, a topic that is usually referred to as photometric redshifts (hereafter photo_z). This problem is distinct from all other estimates of physical properties (stellar mass, star-formation rate, mass of dust and gas, age and star-formation history of the galaxy) because independent and more precise measurements of the same property are available for large samples in the form of spectroscopic redshifts (assuming some cosmological model). The method can thus be tested extensively and even calibrated empirically. It is also historically one of the earliest forms of SED fitting, having been suggested as a manner to go beyond the limits of early spectroscopy [Baum, 1957].

We performed our own analysis using the first set of data that we got in the SHELA region [Papovich et al., 2016]. It covers $\approx 24 \text{ deg}^2$ and contains over 1,800,000 sources. We perform cross-matching between our catalog and SDSS DR14 release using SQL Query CasJobs. The table "SpecObj" contains data from all available SDSS spectroscopic catalogs. There are 15,790 sources in our catalog that are identified in SDSS DR14 and have spectroscopic redshift. We used this sample to test photometric redshifts produced by three different SED fitting codes - HYPERZ [Bolzonella et al., 2011], LePhare [Arnouts and Ilbert, 2011] and EAZY [Brammer et al., 2008].

HyperZ and LePhare produced marginally the same results with the only difference that LePhare does not assign a source with the photometric redshift if the χ^2 value is too high. Our research suggests using information from as many sources as

possible and we turned down LePhare.

Tests of EAZY reveal not just the tighter correlation between spectroscopic and photometric redshifts, but also significantly smaller CPU time. EAZY works approximately 10 times faster and computes redshifts for a catalog that contains 50 thousands sources in 10 minutes. Considering the size of our catalog, EAZY was a natural choice for the photometric redshift determination.

We observe an unusual scatter in our data around redshift $z \approx 0.4$ when comparing to the spectroscopic sample. Similar behavior can be seen in See Fig.4 in Bundy 2015 [Bundy et al., 2015], fig7 in Rowan-Robinson [Rowan-Robinson et al., 2008] and Fig.11 in Brammer et al. [Brammer et al., 2008]. SED fitting technique depends on strong features in the SEDs of the objects, such as the Balmer break, strong emission lines or even PAH features [Negrello et al., 2009]. We try to investigate the nature of such scatter. It may not be due to the misidentification of the Lyman break as the Balmer/4000A break because we have very few galaxies with $z > 1$ in our sample. Next, we examined the possibility that strong emission lines can alter the redshift. We downloaded SDSS DR14 data for certain emission lines and used flux and emission width of O[II], O[III] and Halpha lines. We compared two sets of galaxies around $z=0.4$ - the one with correct identification of the photometric redshift and the other that has severe offset. We did not observe any correlation between deviation of the photometric redshift from spectroscopic one and the strength of any lines.

FIGURE TO APPEAR LATER.

This scatter can be slightly reduced by rejection of some template available for SED fitting, but there is not strict justification for choice of any particular template that is rejected, so we did not proceed in this way. We claim that such scatter in redshift determination should not affect our main results and we address this issue in the next chapter (binning).

4.1.2 EAZY and FAST

We used EAZY code to compute photometric redshifts based on optical and near-IR fluxes that we accumulated in our catalogs. EAZY [Brammer et al., 2008] is photometric redshift code which was written for samples with incomplete and/or biased spectroscopic information. The code combines features from various existing programs: the possibility of fitting linear combinations of templates (as done in GREGZ), the use of priors (as first done in BPZ), and a user-friendly interface based on HYPERZ. The default template set and the redshift-magnitude priors are derived from semi-analytic models. These models are, of course, only an approximation of reality, but their full completeness down to very faint magnitudes outweighs their imperfect representation of the real Universe. Along with extremely high performance, EAZY has a very flexible interface. Calculation of the photometric redshifts is made based on the linear combination of templates. We used the latest available set of templates (v1.3) provided by Brummer on GitHub². These templates take into account presence of emission lines (H α , H β , OIII, OII, and Ly-alpha) in the following way: SFR is estimated from the template "luminosity" at 2800 Å and then Kennicutt-Schmidt (KS) [Schmidt, 1959], [Kennicutt, 1998] relations are used to add emission lines with fixed line ratios. Another template in this set is an evolved Maraston 2005 SSP, added because it was found that the reddest EAZY template didn't quite get red enough for massive old galaxies at $z < 1$. Two last templates add old and dusty template (Brammer, in prep, 2014) and blue, high equivalent width line template based on [Erb et al., 2010] for low-z galaxies.

Run of the whole set of objects on cluster with EAZY takes less than four hours, so we were able to perform it multiple times, tuning parameters for the better estimation of the photo_z. We used z_m1 - the redshift marginalized over probability distribution

²https://github.com/gbrammer/eazy-photoz/blob/master/templates/eazy_v1.3.spectra.param

$p(z | C)$, where z is a redshift and C - color of the source

Results are compared against available SDSS DR14 spectroscopic data. On Figure 4.1 we plotted the our results in two different fashions: photo_z vs spec_z (top) and a difference between those two results against spec_z (bottom).

We provide the full list of EAZY parameters in Appendix.

4.1.3 Reliability of IR data

It is well known that template errors in the rest-frame near-IR can lead to degraded photo-z performance when near-IR data is included (e.g., Brammer et al. 2008). [Bundy et al., 2012] demonstrated acceptable photo-z performance with near-IR synmags included as a way of validating the synmag methodology. They confirm that the addition of UKIDSS photometry here does not improve the template photo-z results, but also does not degrade them if photometry is appropriately weighted to take template errors into account.

We perform another run of EAZY with only optical photometry provided as input and compare the standard deviation of spec_z vs photo_z. As can be seen in Figure 4.2 near-IR filters do not significantly change the accuracy of the redshift estimation.

4.1.4 Stellar masses

FAST (Fitting and Assessment of Synthetic Templates) [Kriek et al., 2018] is originally an IDL-based code that fits stellar population synthesis (SPS) [Bruzual and Charlot, 2003] templates to broadband photometry and (or) spectra. FAST is compatible with EAZY when fitting broadband photometry - it uses the photometric redshifts derived by that code as an input redshift. IDL (Interactive Data Language), is a programming language used for data analysis. IDL requires a license and is not installed on MU cluster machines so instead we used FAST++, a C++ version of

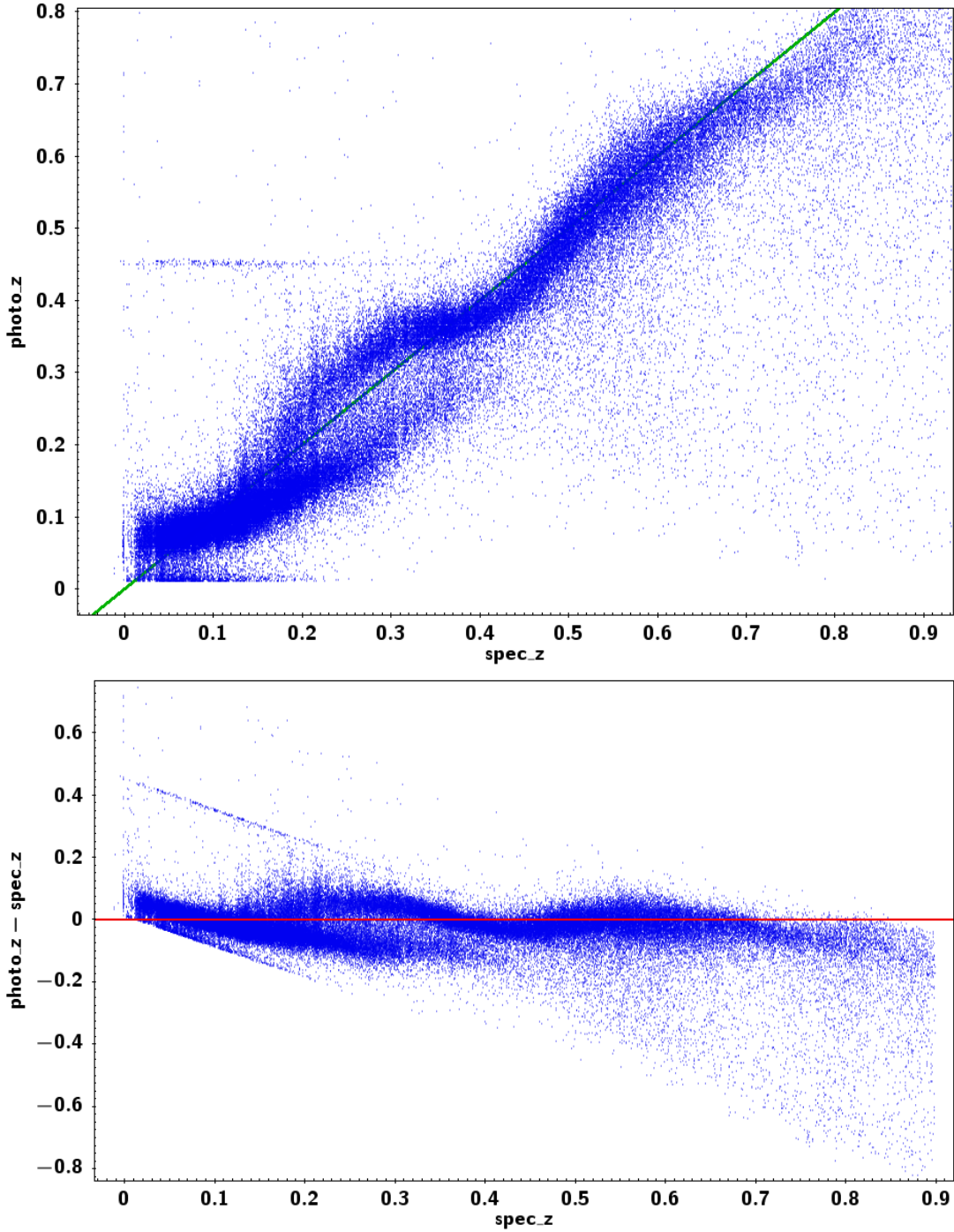


Figure 4.1: Comparison of photo_z as calculated in EAZY to the spec_z from the SDSS spectroscopic data. photo_z vs spec_z is plotted on top, another version of this plot, $\text{photo_z} - \text{spec_z}$ vs spec_z is plotted at the bottom. Despite several observable issues (especially around $z \approx 0.4$) the overall fit is satisfying with the standard deviation as low as $\sigma = 0.07$.

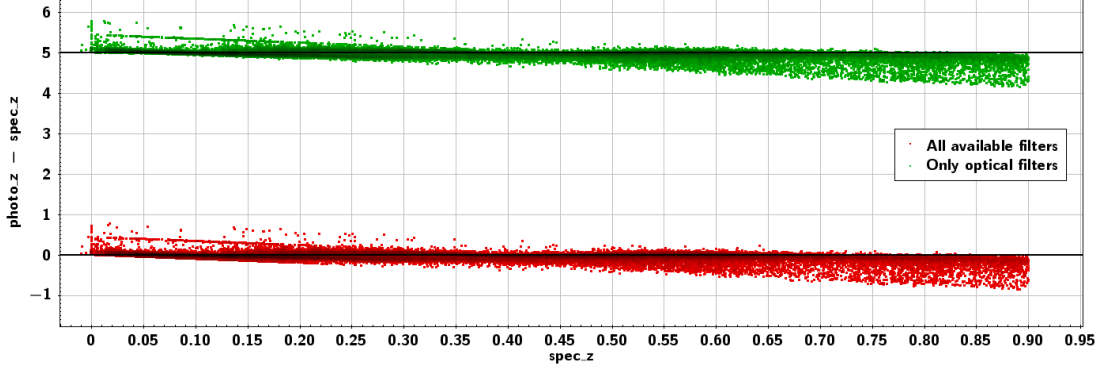


Figure 4.2: Difference of photo_z and spec_z is plotted against spec_z . Data obtained with all 7 or just 5 optical filters are plotted in red and green respectively.

FAST that can be found at [GitHub³](https://github.com/cschrreib/fastpp). FAST++ code uses same input and output formats as FAST, is at least 4 times faster and apart from the single-threaded FAST is multithreading - it may use a number of concurrent threads (CPUs) that the program can use to speed up calculations. Total speed up factor when using C++ and multithreading can be up to 60, which is a significant advantage when working with a data sample as large as ours. We tried several combinations of codes such as:
 HyperZ for redshift estimation and FAST for stellar mass estimation;
 HyperZ for redshift and stellar mass estimation;
 EAZY for redshift estimation and HyperZ for mass estimation;
 EAZY for redshift estimation and FAST for mass estimation;
 and found the last option to be working best. So after we got photometric redshifts for all sources in our catalog with $\text{SNR} > 5$ and non-zero flux in more than 4 filters, we supplied it along with the flux in μJy to the FAST code. It takes around 12 hours CPU time to calculate masses for a set of $\approx 60,000$ sources, so we used Lewis computational cluster again. We present the mass histogram for all four redshift bins on Figure 4.3. We see that galaxies in the lowest redshift bin are on average less massive then and tend to have stellar mass of $\sim 10^{8.8} M_{\text{sun}}$, while galaxies in the higher redshifts peak around mass of $10^{10} M_{\text{sun}}$. This is can be explained by the incompleteness

³<https://github.com/cschrreib/fastpp>

of our sample in high redshifts.

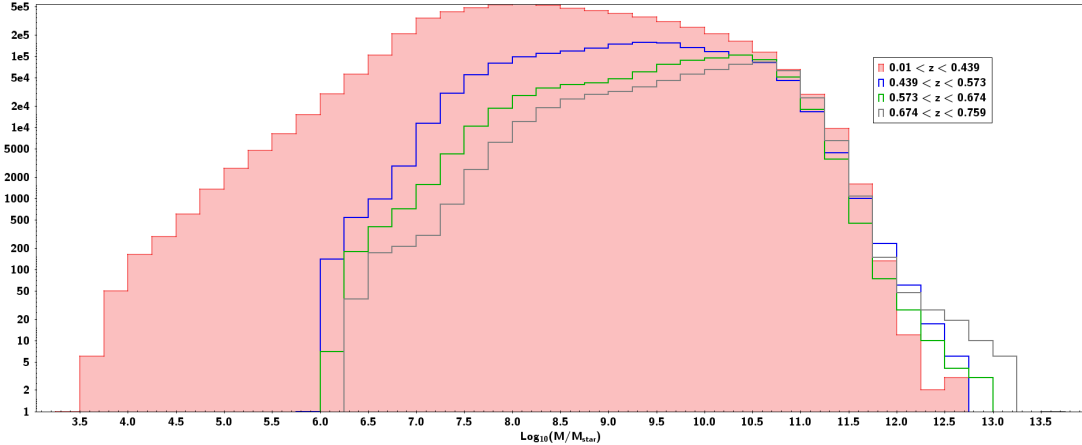


Figure 4.3: A histogram of masses for all four redshift bins. Galaxies in different bins tend to peak at different masses, but galaxies in three high-redshift bins have the highest number of galaxies around similar stellar mass - 10^{10}

4.2 Catalog post-processing

At this point every source that has photometry in more than 4 filters has `photo_z` and stellar mass assigned to it. But this data sample is not clean - there are stars, QSOs, also there are duplicate sources and sources with unreliable near-IR photometry due to the presence of nearby saturated sources. In the following subsections we explain our strategy of constructing the clean sample of galaxies.

4.2.1 Star-galaxy separation

Performing the classification of the sources is an important step in our project. Indeed, SED fitting codes may take photometric data of the star as a valid input and assign it some photometric redshift and stellar mass that does not have any physical significance (χ^2 value of such objects is usually low, but this criteria is not enough to rejects stars). Such objects may severely alter the global density of objects and

skew our results. In this section we attempt to find select galaxies alone from our sample and reject stars and other sources (mainly QSO) that are not a part of this project. Such selection is usually referred to as a "star-galaxy separation". One of the standard ways of performing this separation is via color-color diagram, on which stars and galaxies (hopefully) occupy different space on the graph. We tested several combination of bands in order to achieve best results (i.e. maximum possible number of galaxies rejected and minimal number of non-galaxies included in the sample) and found out that " $w1 - i$ vs $i - z$ " colors works best. As can be seen on (Figure 4.4), galaxies (blue), stars (red) and QSO (green) indeed occupy different space but with large overlapping regions, so the data set will neither be clean, nor complete. Another complication is that while we used r-band as a detection for the optical catalog and so all optical sources have consistent photometry in all 5 bands, some sources are shallow or undetected in w1 band. Such sources are assigned with $w1_mag=99$ and thus occupy a low-left part of this diagram, outside of the reasonable regions.

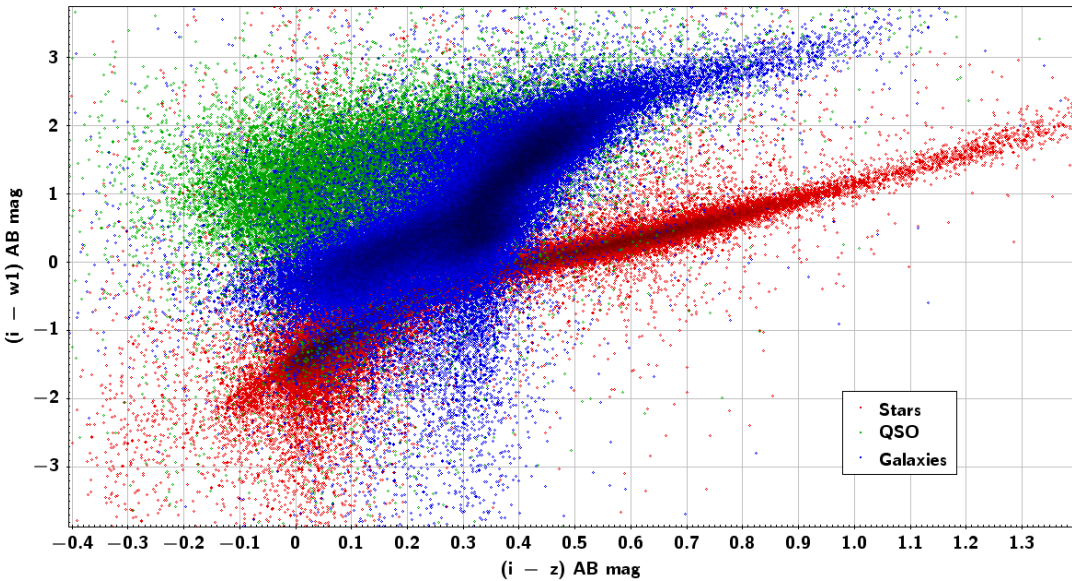


Figure 4.4: Color-color diagram for star-galaxy separation using " $w1 - i$ vs $i - z$ " colors. Galaxies are plotted in blue, stars - in red and QSO in green. It is impossible to create a clean data sample using only colors as a selection criteria.

Lack of IR data for some objects is a real disadvantage of the star-galaxy separa-

tion based on the color-color diagram, so we shall use another approach that is based on the "CLASS_STAR" value - a stellarity index given by **SExtractor**. Stellarity values near "0" indicate the object is likely a galaxy. If stellarity values near "1" that is a good indicator that an object is likely a star. To classify objects, **SExtractor** uses a neural network which takes into account object attributes including FWHM. So the outline of our algorithm is as follows: the PSF functions that we built for every SDSS image will be used to measure FWHM of this image using `irif/psfmeasure` task. Then this FWHM shall be supplied to the parameter file of **SExtractor** and another run of this code is performed in g-, r-, and i-bands (these bands are the most sensitive and generally have better FWHM over u- and z-bands).

Star-galaxy classification based on the CLASS_STAR parameter that is measured in one band is about 95% accurate (Figure 4.5). We attempt to refine this result by finding the combination of selection criteria in three bands instead of just one. We downloaded SDSS DR14 BOSS and SDSS spectrograph data in Stripe 82 region using **CasJob Server**⁴. The size of this data set is 269,196 sources, each of which is assigned with spectroscopic class (can be GALAXY, QSO, or STAR) and extragalactic objects galaxies and QSO are also assigned with the spec_z larger than 0. By matching this catalog to our main output catalog we got a set of data that contains 248,682 sources, which will serve as a training set for our star-galaxy separation. We found the next criteria to perform the best way: $CLASS_STAR_r < 0.2 \quad \&\& \quad CLASS_STAR_g < 0.34 \quad \&\& \quad CLASS_STAR_i < 0.70$

After this criteria has been applied to the data set we found that 3,874 galaxies (1.55%) fall outside of the catalog and 4298 (1.73%) stars and QSO are included into the sample (Figure 4.5). We are satisfied with this result and perform the above criteria to the whole data set that decreases our total number of sources from 26,585,975

⁴<https://skyserver.sdss.org/CasJobs/>

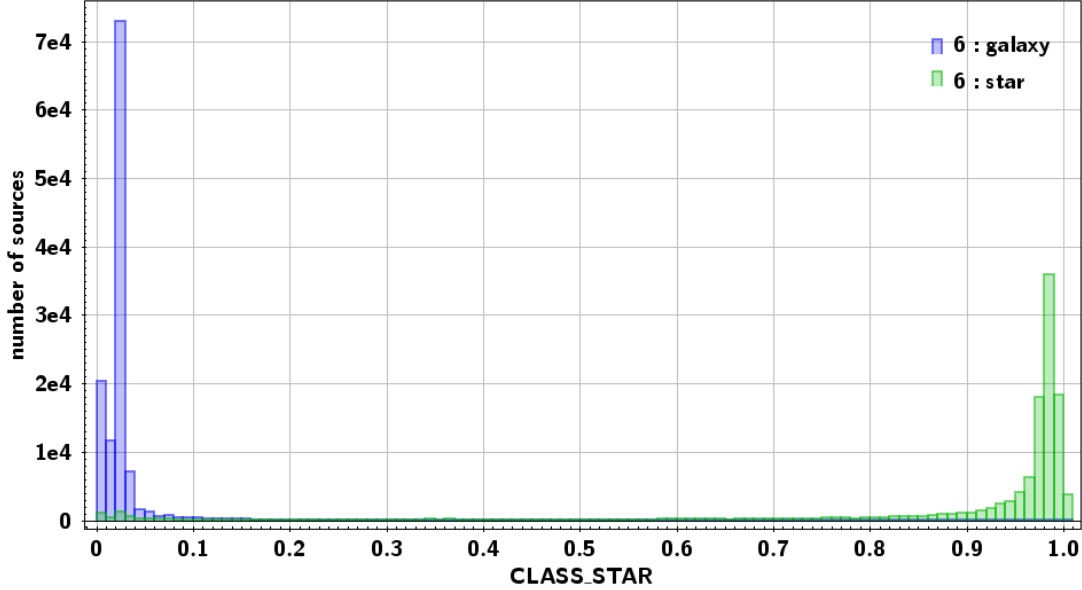


Figure 4.5: A histogram of the CLASS_STAR values for r-band alone already shows efficiency of this method for star-galaxy separation. Galaxies and stars are selected from BOSS spectroscopic survey using parameter "CLASS". Galaxies are plotted in blue and tend to have smaller values of CLASS_STAR, stars are plotted in green and mostly have CLASS_STAR value close to 1.

to 10,092,410 objects.

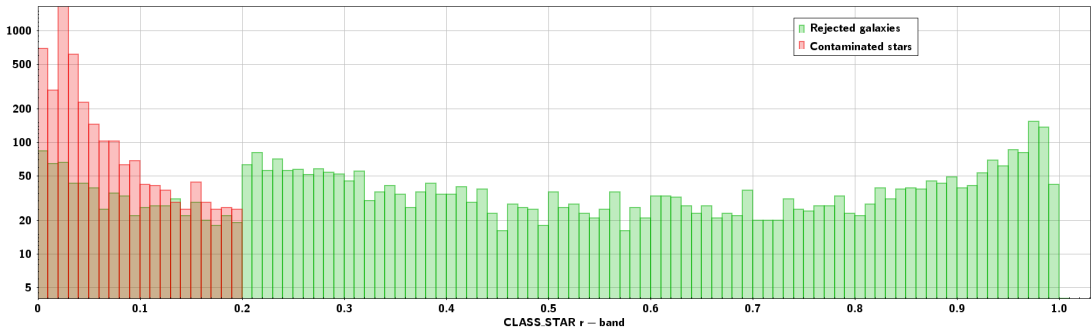


Figure 4.6: A histogram of the CLASS_STAR values for galaxies from the control data sample that are rejected from our data sample due to very large CLASS_STAR values (green). In red we plotted stars and QSO that are not excluded from our data sample - their CLASS_STAR values are too small in all three optical bands that we used for star-galaxy separation.

4.2.2 Sources treatment in overlapping regions and around bright stars

Two adjacent SDSS images have overlapping regions - $25''$ wide for images in the same columns (i.e. their centers have the same Dec) and $28''$ wide for images in the neighbor columns (i.e. their centers have the same RA). Sources that appear in such regions are **SExtracted** and **TPHOTed** twice and have to be removed from the final catalog. We perform internal match on the catalog within all 80 unWISE frames and remove duplicate sources within 1.2 asec matching radius using **STILTS** code. We verify that this radius is sufficient for removing majority of duplicate sources and also does not remove any non-duplicate sources in the main field that may have similar coordinates. This operation reduced the number of galaxies in our sample to 9,308,387 sources. An example of such duplicate sources is plotted with blue on Figure 4.7

One unWISE frame consists of 3 unWISE images that have the same RA and are centered at Dec= -1.6^0 , 0.0^0 and $+1.5^0$. When we plotted SDSS images over unWISE frame, we noticed that each SDSS image from col07 and unWISE file that is centered at Dec= $+1.5^0$ overlap in a small region ≈ 52.28 square minutes. To process this small area in TPHOT another 2,315 PSFs have to be constructed. We decided not to perform this very time-consuming operation and exclude this area, in total 5.55 deg^2 from our project. The same situation is with SDSS images from col02 and unWISE files centered at Dec= -1.6^0 . Total area that was excluded from the project is 11.340 deg^2 , it may be seen as two white horizontal stripes on Figure 4.7

Objects that are extremely bright in near-IR present a number of problems to the photometry measurement by generating a host of artifacts. These artifacts include halos (low surface brightness emission extending well beyond the PSF), diffraction spikes, horizontal stripes and residual ghosts. If not corrected, these artifacts will compromise the reliability of w1 and w2 photometry performed by TPHOT. To ac-

count for such artifacts the natural solution is to mask certain regions based on available catalogs. We used SAO star catalog [Staff, 1966] and Bright IR Stars Compilation (BIRSC) [R. Tam and C. Xu - IPAC] as a base for the masking catalog. There are around 400 stars in both catalogs that fall within Stripe 82 footprint, but our visual inspection showed that some very bright objects (stars and galaxies) that severely alters results of TPHOT are not in this list. We inspected all residual FITS images and added 300 more objects to the list that now consists of 706 objects. For stars from the catalog the masking area depends on the provided V-band magnitude and it was assigned manually based on the estimation of the halo for the added objects. Radii for masking are ranging from 50 to 500 arcsec. An example of such source with masking radius=100 asec is presented on Figure 4.8. The overall masked area is 3.871 deg^2 , which reduces the total sky area of the survey to 288.212 deg^2 .

After rejection of such objects our catalog contains 9,061,068 objects and this is the final sample that we use as input to SED fitting codes that return `photo_z` and stellar mass that we use to build GSMD.

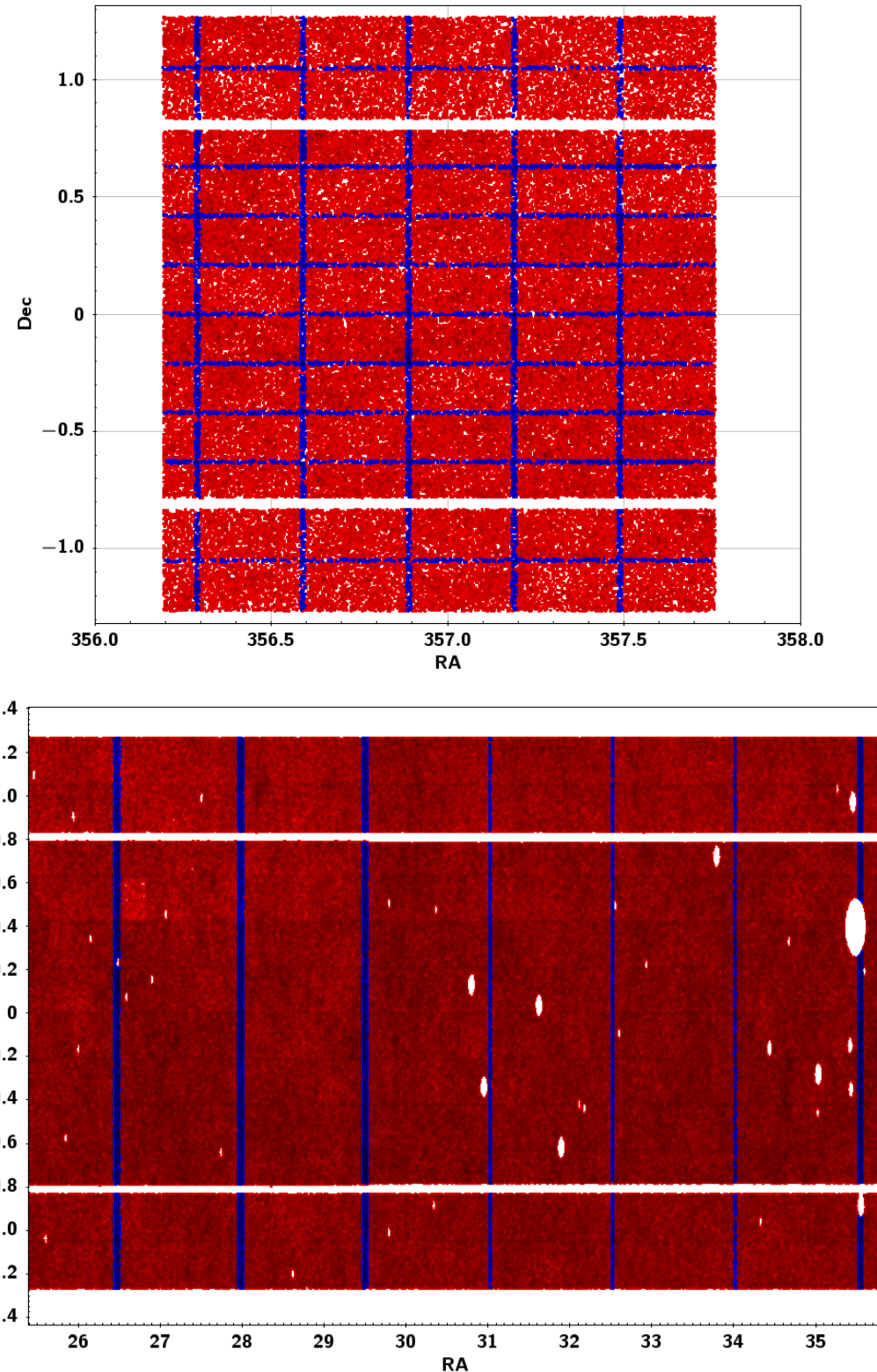


Figure 4.7: Duplicate sources (blue) are over-plotted with unique sources (red) in one unWISE frame that hosts 72 SDSS images (top image) and several adjacent unWISE frames (bottom image). Two white horizontal stripes between col07 and col02 (bottom) and col11 and col06 (top) were also excluded from our project.

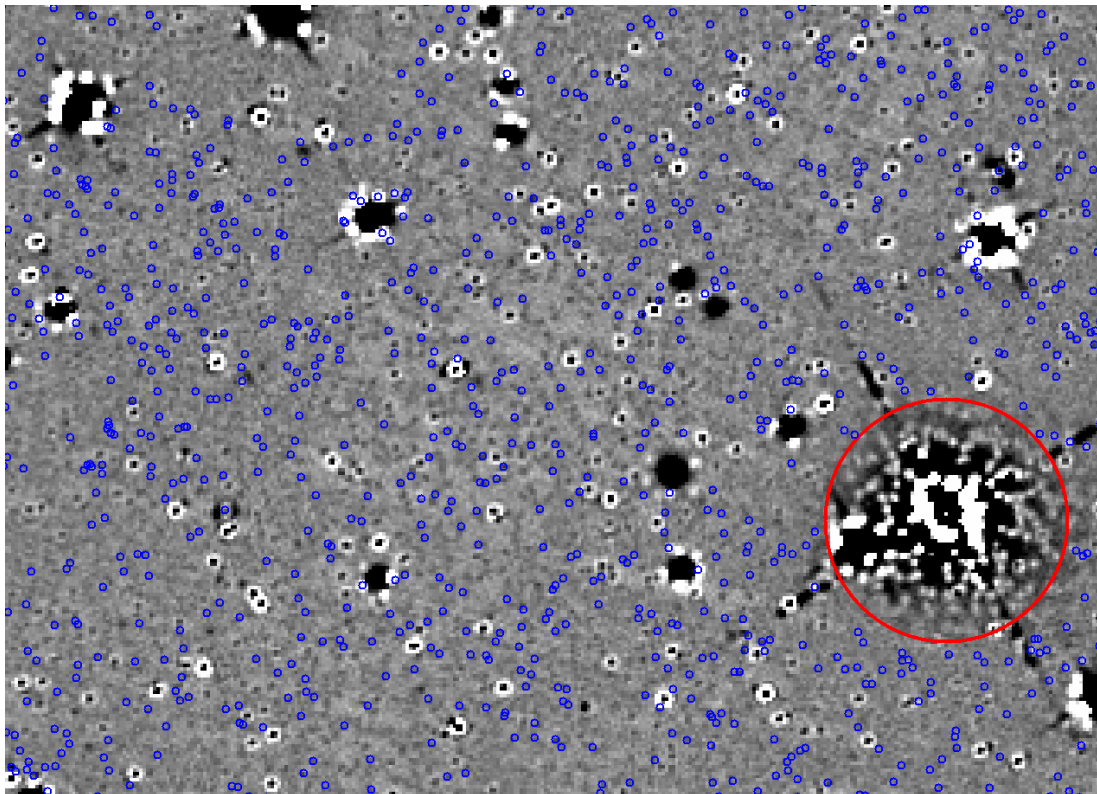


Figure 4.8: Residual image in w1 band with various regions plotted. All sources that were detected in r-band and supplied to TPHOT, but fall within the masked region (red) are excluded from the SED fitting. Blue circles 3 asec in radius show the position of objects, whose flux was subtracted from the unWISE image. Poorly subtracted objects (mostly stars) without blue circles around them were included into TPHOT input catalog, but later were excluded from ED fitting after star-galaxy separation

Chapter 5

Results

5.1 Binning in redshift

Stellar mass density is calculated within some volume, so we bin our sample to four redshift intervals of the same physical volume - $139,729,000 Mpc^3$. The size of the bin is chosen the way that we still have sufficient sources in the highest redshift bin - even though our photometric redshifts span up to $z \approx 0.9$, the number sources at this redshift decreases significantly and this incompleteness leads to the severe underestimation of the number density. Information about binning is presented in Table 5.1. Although it is tempting to create larger number of bin in order to see evolution of the stellar mass at "high-resolution", we remember that our redshift is determined based on photometry and thus is not reliable within better than $\Delta z \approx 0.1 - 0.15$ (also recall large scatter around $z \sim 0.4$). So we decided to have four large bins in which errors in redshifts and associated stellar masses shall be averaged. Stellar mass is plotted against photo_z in all four bins on Figure 5.1.

We sum up stellar mass of all galaxies in a bin and divide it by the bin volume to derive the stellar mass density per bin in units of M_\odot/Mpc^3 . Stellar mass density

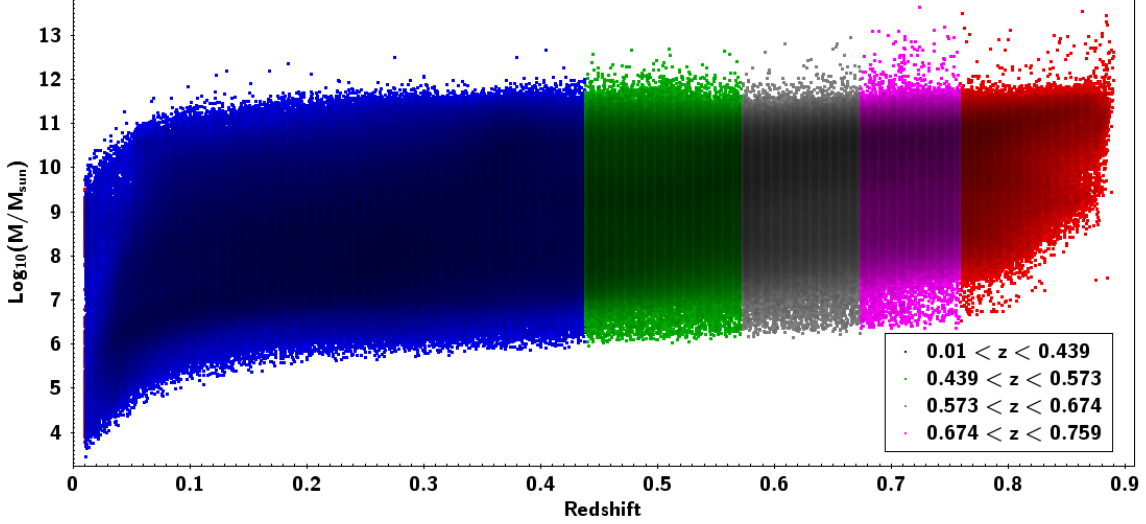


Figure 5.1: Stellar mass density over photometric redshift. Four redshift bins are plotted in different colors: z1 - blue, z2 - green, z3 - grey, z4 - magenta. Red sources at $z > 0.759$ are not included into the sample due to their low number density.

Table 5.1: Redshift binning of stellar mass

#	redshift interval	mean redshift	# of galaxies per bin	fraction of galaxies per bin
1	$0.010 < z < 0.439$	0.296	6,065,140	0.65
2	$0.439 < z < 0.573$	0.506	1,588,509	0.17
3	$0.573 < z < 0.674$	0.623	812,562	0.09
4	$0.674 < z < 0.759$	0.716	585,009	0.06

is usually represented in a log scale. Also, in order to compare our results to other published data we scaled from a Chabrier IMF to a Salpeter IMF by multiplying the stellar masses by a factor of 1.64. Results are combined in Table 5.1 and will be published in [Musin and Yan \[in prep.\]](#).

Table 5.2: Stellar mass density

#	redshift interval	total mass	$\log_{10}(\rho)$ Chabrier IMF	$\log_{10}(\rho)$ Salpeter IMF
	z	M_\odot	$\log_{10}(M_\odot/Mpc^3)$	$\log_{10}(M_\odot/Mpc^3)$
1	$0.010 < z < 0.439$	$2.785 \cdot 10^{16}$	8.299	8.514
2	$0.439 < z < 0.573$	$1.671 \cdot 10^{16}$	8.077	8.292
3	$0.573 < z < 0.674$	$1.569 \cdot 10^{16}$	8.050	8.265
4	$0.674 < z < 0.759$	$1.718 \cdot 10^{16}$	8.089	8.304

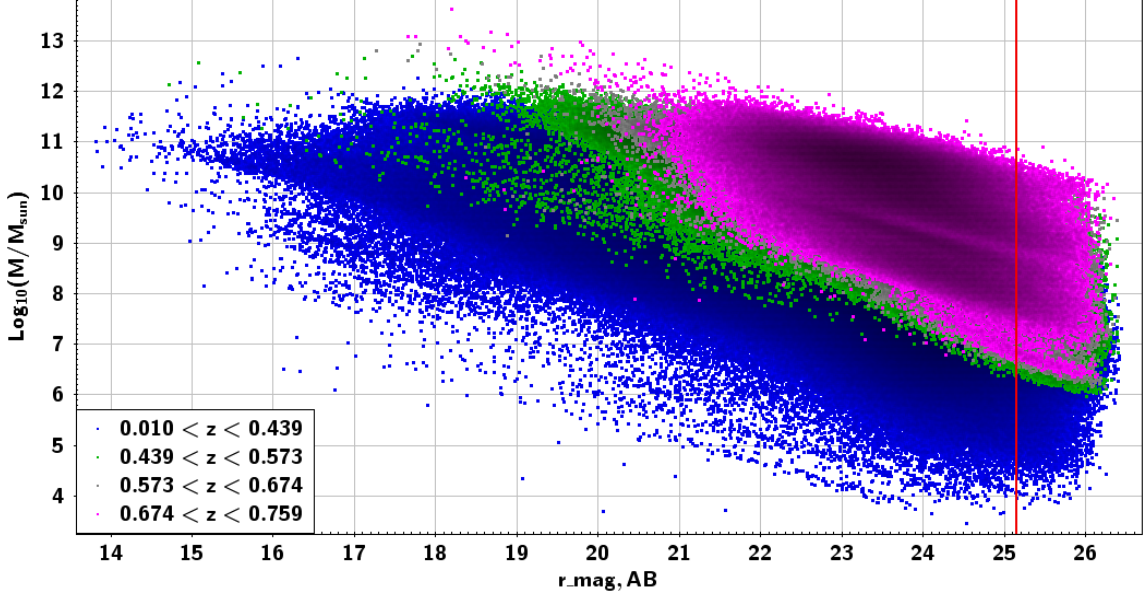


Figure 5.2: Stellar masses are plotted over corresponding r-band magnitudes. Four redshift bins are plotted in different colors: z_1 - blue, z_2 - green, z_3 - grey, z_4 - magenta. Red vertical line denotes the 3σ detection limit.

On the Figure 5.2 we present stellar masses, binned to four redshifts as a function of r-band magnitude. Red vertical line shows the 3σ detection limit for the r-band. It does not necessarily mean, that we should not trust masses beyond this limit as those sources may have reliable photometry in other bands, but it should at least be taken with caution.

5.2 GSMD and comparison to the results of other groups

In their review paper Madau & Dickinson [Madau and Dickinson, 2014] presented a compilation of recent measurements of SMD from different groups up to $z \approx 8$. They used all available data including wide field local SDSS based SMD. We predict that before any corrections our SMD should be somewhat close to reported results. We overplotted derived SMD with green dots with green arrows on top of the figure presented in [Madau and Dickinson, 2014]. As you may see on Figure 5.3 our points

lie very close to some of the reported data, especially to [Bielby et al., 2012], who used J,H and Ks filters to investigate the SMD in four CFHTLS deep fields.

Our reported mass density for the fourth redshift bin, $0.674 < z < 0.759$ (8.089) is higher than that for the third one, $0.573 < z < 0.674$ (8.050). It may not be a representation of any real processes, because even though generally stellar mass in a certain small volume can go down due to the end of the life cycle of massive stars, in general galaxies tend to increase their stellar mass in time. Interestingly, the same behavior is observed in the data of other groups, as can clearly be seen on Figure 5.3 in the region denoted by red rectangular. We interpret this "wiggle" in two ways - as a direct evidence of the incompleteness of our data sample or as a systematic overestimation of stellar masses in the highest redshift bin (some galaxies are assigned with stellar masses as high as $10^{13} M_{\text{sun}}$, which is not supported by any observations of galaxies at such redshifts).

The problem of incompleteness appears in any survey, photometric or spectroscopic - low-mass galaxies at higher redshifts are too dim to be detected. Correction for incompleteness is beyond the scope of this thesis and we only outline here the possible approach. This incompleteness can be estimated based on a comparison to the much deeper small area surveys or based on the analytic correction that can be applied using the available data from Figure 5.1.

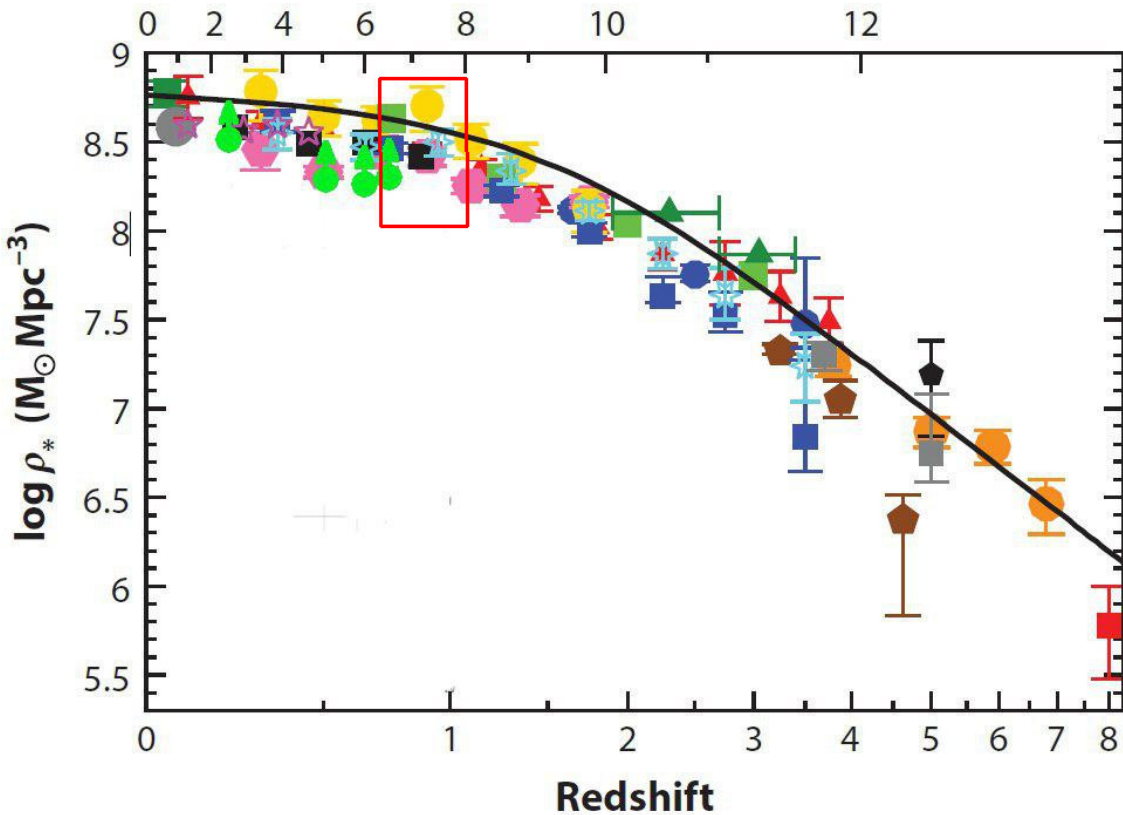


Figure 5.3: Figure 11 from Madau&Dickinson. 2014 with our SMD data points plotted as low-limit with green dots with arrows. Data points inside the red rectangular demonstrate an odd "wiggle" upwards as if the SMD was higher in the earlier Universe

Chapter 6

Summary and concluding remarks

6.1 Conclusions

In this thesis we investigated the evolution of galaxies by studying the growth of stellar mass and stellar mass density in time in the last 6 Gyr. We combined the datasets from two very large surveys and built the largest catalog of galaxies to date that has consistent fluxes in 5 optical (SDSS) and 2 near-IR (WISE) bands and contains over 9,000,000 galaxies. This consistency has been achieved in two ways:

- in optical all bands were convolved with the PSF of the band with the worst FWHM, namely u-band. We did this by constructing PSF functions for each individual SDSS image. Then, using r_matched_u band as a detection image we extracted fluxes of the sources in SDSS Stripe 82 field.
- in near-IR the angular resolution is ≈ 6 times worse than in optical, so we applied "template-fitting" technique in which we use the high-resolution image to define the morphological template of the galaxy in question, and de-convolve its light profile in the low-resolution image.

This approach allows us to perform SED measurements in the restframe near-

IR regime, which is important for the correct estimation of the dust extinction and contribution of the low-mass stars, which may be outshone by brighter stars in optical, and thus are accountant, but contribute a significantly to the total stellar mass of the galaxy. We derive photometric redshifts and stellar masses for all the 9 million galaxies that span $z = 0\text{--}0.8$ and calculated stellar mass density over four redshift bins. Our SMD (we call it low-limits, since we did not correct for incompleteness of low-mass galaxies in the higher redshift bins) are generally close to the previously reported results, but with a much larger statistics over significant portion of the sky. Our result contribute to the GSMD and shall be used in future to provide constraints on any models of the galaxy evolution at high redshifts.

6.2 Future work

In 2010, after the depletion of coolant, w3 and w4 became unusable. Nevertheless, WISE continued surveying the sky through 2011 January in w1 and w2 as they are less affected by the rising temperature of the sensor, including a portion of the mission referred to as NEOWISE [Mainzer et al., 2011]. WISE was placed in hibernation in 2011 February, and was later reactivated in 2013 October and continued surveying the sky in w1 and w2. This survey is referred to as NEOWISE-Reactivation (NEOWISER) and continued until 2017. NEOWISER images are of very nearly the same high quality as those of the pre-hibernation WISE mission and it was quickly appreciated by the astronomical community. [Meisner et al., 2017] created a set of co-add images following procedures in [Lang, 2014] for all available data in bands w1 and w2. This not only made the images more sensitive (by 0.38 magnitudes in both bands), but significantly reduce the noise and allowed to clean out transient and spurious sources. That is very important to us because as you may see in the Figure 6.1 lots (58%) of the sources are below the detection limit. We still supply such sources to

TPHOT for the reasons to be explained in the next subsection, but their magnitudes are untrustworthy. New data from [Meisner et al., 2017] will add 5% more percents of sources above the detection limit and make stellar mass estimation more robust.

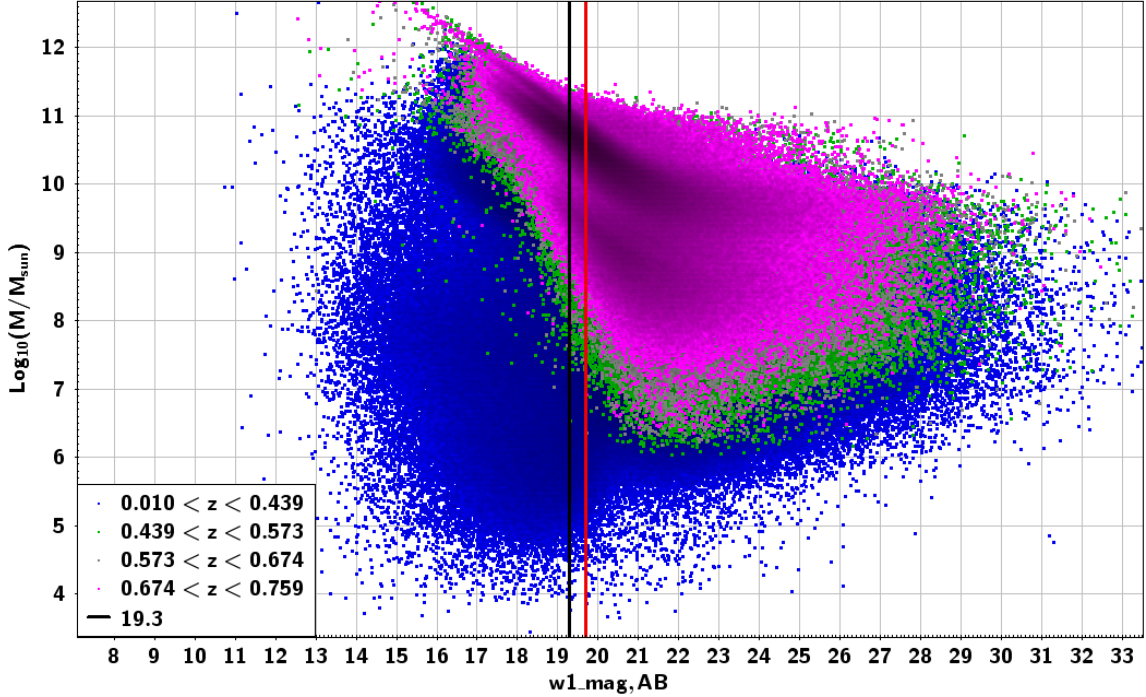


Figure 6.1: Stellar masses are plotted over corresponding w1-band magnitudes. Four redshift bins are plotted in different colors: z1 - blue, z2 - green, z3 - grey, z4 - magenta. Black vertical line denotes the 5σ detection limit for unWISE, red vertical image - analogous detection limit for the stacked WISE and NEOWISER data

In order to use these images we need to construct 240 new PSFs per band (480 in total) convolve them to already existing r_matched_u PSFs and re-run the TPHOT over entire Stripe 82 region. Such run, though time-consuming, will not only significantly increase the precision of the near-IR photometry, but also increase the total number of sources. In deeper near-IR images more sources will have non-zero fluxes - so sources that now have photometric fluxes in less than 4 bands and are currently not supplied for SED fitting will be included in the stellar mass density estimation.

6.2.1 Optical dropouts in WISE

Residuals in w1 and w2 that are produced by TPHOT reveal a mysterious population of objects with $\text{SNR} > 5$ in both bands. The fact that they were not "cleaned out" by TPHOT suggests that they are invisible in optical and our inspection of SDSS images proves this. We call them "WISE optical dropouts" (WoDrops) and investigating their nature is a follow-up for this project, though some preparatory work has been already done.

- Using the latter WISE observations in w1 and w2 during "3-Band Cryo" and "NEOWISE" programs, we verified that these objects cannot be transients.
- Their colors ($w1 - z > 4.8$ AB mag) cannot be explained by Galactic brown dwarfs.
- WoDrops cannot be a high-redshift ($z > 7$) objects due to their large number density ($\tilde{176}/\text{square degree}$) - that contradicts to current observations of the population of the most luminous quasars.

An example of such WoDrop is presented in Figure 6.2

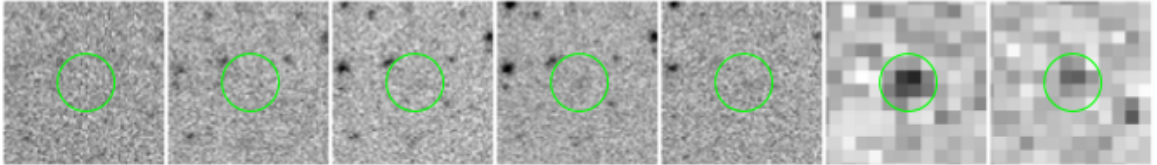


Figure 6.2: An example of WoDrop. Shown from left to right are the *ugriz* and unWISE w1 and w2 images. The images are $33'' \times 33''$ in size, and the green circles indicate the location of the WoDrop. For this particular example is $\text{SNR} = 8$ and 5.4 for bands w1 and w2 respectively.

The only reasonable explanation is that these objects may be a low-redshift ($z \sim 0.5$) old, massive but passive galaxies that resemble in colors Spitzer IRAC-selected Extremely Red Objects (IERO) [Yan et al., 2004]. If this is really the case then our low- z stellar mass density may be underestimated. In order to better understand the nature of such objects we need data in the near-IR regime, namely filters J, H and Ks - they lie in between optical filters *ugriz* and w1, w2 bands. Figure 6.3 shows an

example of the SED fitting for one of the WoDrops. W1 and w2 photometry is shown in magenta, non-detection in optical bands is plotted with upper-limits in grey and possible photometry for J, H and Ks bands is in blue.

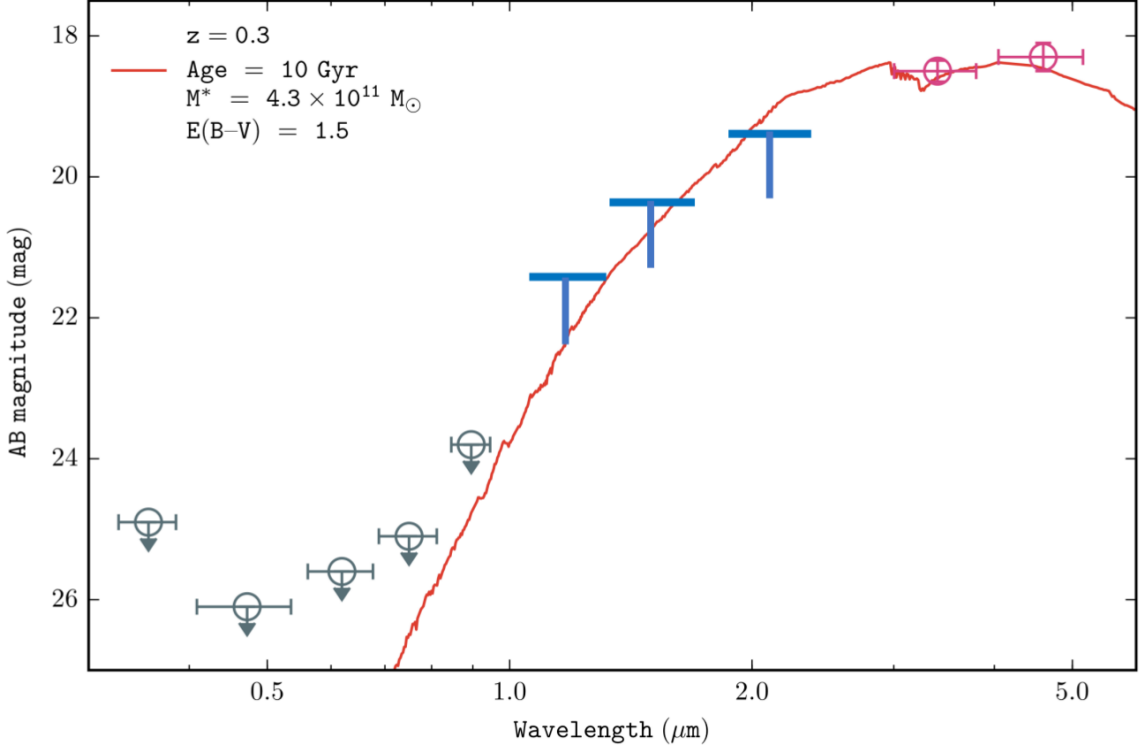


Figure 6.3: Illustration of the probable explanation to the nature of WoDrops. The photometry of this object in w1 and w2 are indicated by the two magenta points, and its non-detection in the Stripe 82 *ugriz* images is indicated by the 2σ upper limits shown in grey.

To date only quarter of the Stripe 82 footprint has been searched for the presence of WoDrops. We expect to find $\approx 52,800$ dropouts. Creating the full set of WoDrops requires careful visual inspection of thousands of images, is extremely time-consuming but shall be completed in the nearest future.

We used several opportunities to add complementary photometric data to catalog. A fraction of sources is detected in IRAC SHELA - a 24 square degree survey at 3.6 and 4.5 microns [Papovich et al., 2016]. This survey is complete to 22.0 AB limiting magnitude but covers less than 10% of Stripe 82.

Five objects were observed with WIYN High Resolution Infrared Camera (WHIRC)

[Smeet et al., 2011]. Figure 6.4 shows that results are contradictory - after 3 hours of the total integration time per source only one source has detection in H and Ks, but not in J. All other sources are undetected. This non-detection is even a more interesting result as it may be a signal of detecting a new population of objects.

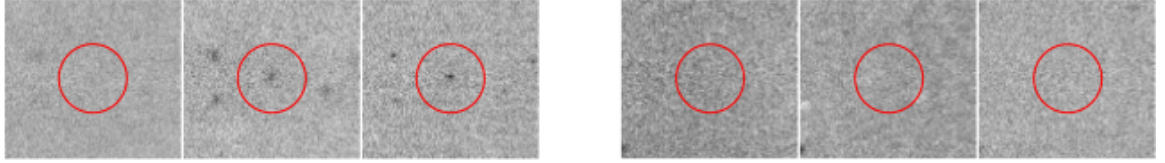


Figure 6.4: An example of two WoDrops that have been observed by near-IR imager WHIRC instrument at WIYN telescope. All images are $33''33''$ in size, and the red circles indicate the location of the WoDrop. The nominal on-source exposures are 31 min, 43 min and 1.1 hrs in Ks, but as can be seen, one WoDrop is only detected in H and Ks band, while the second one is not detected (as well as other three WoDrops that were observed in this run)

To further investigate the nature of these objects, an observing proposal was submitted to the Large Binocular Telescope (LBT) telescope to observe another 20 WoDrops (LBTO Reference: TS-2018B-006, PI - Haojing Yan). This 8m class telescope is equipped with LUCI (originally LUCIFER) - Large Binocular Telescope Near-infrared Spectroscopic Utility with Camera and Integral Field Unit for Extragalactic Research. LUCI operates in the 0.9 - 2.5 micron spectral range and provides imaging and spectroscopic capabilities in seeing- and diffraction limited modes.

ACKNOWLEDGMENTS

I would like to thank my academic adviser, professor Haojing Yan for his tremendous support and patience, *support and patience*.

I would like to extend my sincere gratitude to all the professors from the Physics Department of University of Missouri, particularly to professor Sergei Kopeikin, professor Bahram Mashhoon and professor Angela Speck.

This thesis would not have been even started without my beloved parents, and certainly would not have been finished without support, help and love from my wife, Kristina Ulasovich.

I would particularly like to thank my grandmother, Razia Akhtyamova who taught me to look above the ordinary things and never stop dreaming.

Dear Venera Khalikova, the coffee that you gave to me is responsible for some of the most creative chapters of this dissertation.

The computation for this work was performed on the high performance computing infrastructure provided by Research Computing Support Services and in part by the National Science Foundation under grant number CNS-1429294 at the University of Missouri, Columbia, MO.

Appendix A

Parameters for applied codes

A.1 SExtractor parameters for x_matched_u catalogs

```
DETECT_TYPE CCD # CCD (linear) or PHOTO (with gamma correction)
DETECT_MINAREA 3 # minimum number of pixels above threshold
THRESH_TYPE RELATIVE # threshold type: RELATIVE (in sigmas)
# or ABSOLUTE (in ADUs)

DETECT_THRESH 2.5 # <sigmas> or <threshold>,<ZP> in mag.arcsec-2
ANALYSIS_THRESH 2.5 # <sigmas> or <threshold>,<ZP> in mag.arcsec-2
FILTER Y # apply filter for detection (Y or N)?

FILTER_NAME gauss_2.0_5x5.conv # name of the file containing the filter
FILTER_THRESH # Threshold[s] for retina filtering

DEBLEND_NTHRESH 32 # Number of deblending sub-thresholds
DEBLEND_MINCONT 0.005 # Minimum contrast parameter for deblending
CLEAN Y # Clean spurious detections? (Y or N)?
CLEAN_PARAM 1.0 # Cleaning efficiency
```

```

MASK_TYPE CORRECT # type of detection MASKing: can be one of
# NONE, BLANK or CORRECT

WEIGHT_TYPE MAP_WEIGHT,MAP_WEIGHT # type of WEIGHTing: NONE, BACKGROUND,
# MAP_RMS, MAP_VAR or MAP_WEIGHT

WEIGHT_GAIN N,N # modulate gain (E/ADU) with weights? (Y/N)

WEIGHT_THRESH # weight threshold[s] for bad pixels

FLAG_IMAGE flag.fits # filename for an input FLAG-image

FLAG_TYPE OR # flag pixel combination: OR, AND, MIN, MAX
# or MOST

PHOT_APERTURES 9.0 # MAG_APER aperture diameter(s) in pixels

PHOT_AUTOPARAMS 2.5, 3.5 # MAG_AUTO parameters: <Kron_fact>,<min_radius>

PHOT_PETROPARAMS 2.0, 3.5 # MAG_PETRO parameters: <Petrosian_fact>,
# <min_radius>

PHOT_AUTOAPERS 0.0,0.0 # <estimation>,<measurement> minimum apertures
# for MAG_AUTO and MAG_PETRO

PHOT_FLUXFRAC 0.5 # flux fraction[s] used for FLUX_RADIUS

SATUR_LEVEL 25000.0 # level (in ADUs) at which arises saturation

SATUR_KEY SATURATE # keyword for saturation level (in ADUs)

MAG_ZEROPPOINT 00.0

MAG_GAMMA 4.0 # gamma of emulsion (for photographic scans)

GAIN 0.0 # detector gain in e-/ADU

GAIN_KEY GAIN # keyword for detector gain in e-/ADU

PIXEL_SCALE 0.396 # size of pixel in arcsec (0=use FITS WCS info)

SEEING_FWHM 1.5 # stellar FWHM in arcsec

STARNNW_NAME default.nnw # Neural-Network_Weight table filename

BACK_TYPE AUTO # AUTO or MANUAL

BACK_VALUE 0.0 # Default background value in MANUAL mode

```

```

BACK_SIZE 8

BACK_FILTERSIZE 3 # Background filter: <size> or <width>,<height>

BACKPHOTO_TYPE GLOBAL # can be GLOBAL or LOCAL

BACKPHOTO_THICK 24 # thickness of the background LOCAL annulus

BACK_FILTTHRESH 0.0 # Threshold above which the background-
# map filter operates

```

A.2 TPHOT parameters

```

order standard #1st pass

order standard2 #2nd pass

usereal True

usemodels False

useunresolved False

normalize true

subbckg True

savecut false

cutoutdir cutouts

cutoutcat cutoutscutouts.cat

modelscat modelsmodels.cat

modelsdir models

culling false

errtype wht

rmsconstant 1

relscale 7

FFTconv true

```

```
multikernels false
mkext false
kernellookup ch1_dancecard.txt
templatedir templates
templatecat templatestemplates.cat
fitpars tpipe_tphot.param1
tphotcat lores_tphot.cat_pass1
tphotcell lores_tphot.cell_pass1
tphotcovar lores_tphot.covar_pass1
fitting single
cellmask true
maskfloor 1e-9
fitbackground false
fit_loc_bkgd 0
writecovar true
threshold 0.0
linsyssolver lu
clip true
rmscheck 0
modelfile lores_collage_pass1.fits
dzonesize 5
maxshift 0.5
ddiagfile ddiags.txt
dlogfile dlog.txt
dancefft true
nneighinterp 0
```

A.3 EAZY parameters

```
FILTER_FORMAT 1 # Format of FILTERS_RES file -- 0: energy- 1: photon-counting
detector

SMOOTH_FILTERS y # Smooth filter curves with Gaussian
SMOOTH_SIGMA 100. # Gaussian sigma (in Angstroms) to smooth filters
TEMPLATES_FILE eazy_v1.3.spectra.param # Template definition file
TEMPLATE_COMBOS a # Template combination
NMF_TOLERANCE 1.e-4 # Tolerance for non-negative combinations (TEMPLATE_COMBOS=a)
TEMP_ERR_A2 1.00 # Template error amplitude
SYS_ERR 0.00 # Systematic flux error
APPLY_IGM y # Apply Madau 1995 IGM absorption
DUMP_TEMPLATE_CACHE n # Write binary template cache
USE_TEMPLATE_CACHE n # Load in template cache
CACHE_FILE tempfilt.dat # Template cache file (in OUTPUT_DIRECTORY)
NOT_OBS_THRESHOLD -90 # Ignore flux point if <NOT_OBS_THRESH
N_MIN_COLORS 4 # Require N_MIN_COLORS to fit
CHI2_SCALE 1.0 # Scale ML Chi-squared values to improve confidence intervals
APPLY_PRIOR n # Apply apparent magnitude prior
PRIOR_ABZP 23.9 # AB zeropoint of fluxes in catalog.!
FIX_ZSPEC n # Fix redshift to catalog zspec
Z_MIN 0.01 # Minimum redshift
Z_MAX 0.9 # Maximum redshift
Z_STEP 0.01 # Redshift step size
Z_STEP_TYPE 1 # 0 = ZSTEP, 1 = Z_STEP*(1+z)
GET_ZP_OFFSETS n # Look for zphot.zeropoint file and compute zeropoint offsets
H0 70.0 # Hubble constant
OMEGA_M 0.3 # Omega matter
```

```
OMEGA_L 0.7 # Omega lambda
```

A.4 FAST parameters

```
SAVE_SIM = 0 # 0 / 1
SFR_AVG = 0 # 0, 100 Myr, 300 Myr etc
INTRINSIC_BEST_FIT = 0 # 0 / 1
BEST_SFHS = 0 # 0 / 1
SFH_OUTPUT_STEP = 10 # 10 Myr, 100 Myr etc
SFH_OUTPUT = 'sfr' # 'sfr' or 'mass'
REST_MAG = [] # [140,142,161] for UVJ colors
CONTINUUM_INDICES = ''
OUTPUT_COLUMNS = [] # ['id','Av','lmass','lsfr', ...]
LIBRARY = 'bc03' # 'bc03' / 'ma05' / 'co11'
RESOLUTION = 'hr' # 'pr' / 'lr' / 'hr'
IMF = 'ch' # 'ch' / 'sa' / 'kr'
SFH = 'exp' # 'exp' / 'del' / 'tru'
DUST_LAW = 'calzetti' # 'calzetti' / 'mw' / 'kc' / 'noll'
LOG_TAU_MIN = 6.5 # log [yr]
LOG_TAU_MAX = 11.0 # log [yr]
LOG_TAU_STEP = 0.1 # log [yr], min 0.1
LOG_AGE_MIN = 6.0 # log [yr]
LOG_AGE_MAX = 10.2 # log [yr]
LOG_AGE_STEP = 0.1 # log [yr]
NO_MAX_AGE = 0 # 0 / 1
Z_MIN = 0.01 # Cannot be 0.0
```

```
Z_MAX = 0.90
Z_STEP = 0.005
Z_STEP_TYPE = 0 # 0: Z_STEP, 1: Z_STEP*(1+z)
A_V_MIN = 0. # [mag]
A_V_MAX = 1.6 # [mag]
A_V_STEP = 0.05 # [mag]
METAL = [0.02] # [0.0096,0.019,0.03]
NO_CACHE = 0 # 0 / 1
H0 = 70.0 # Hubble constant
OMEGA_M = 0.3 # Omega matter
OMEGA_L = 0.7 # Omega lambda
SAVE_CHI_GRID = 0 # 0 / 1
```

Bibliography

- J. K. Adelman-McCarthy and et al. Vizier online data catalog: The sdss photometric catalog, release 5 (adelman-mccarthy+, 2007). *VizieR Online Data Catalog*, 2276, March 2007. URL <http://adsabs.harvard.edu/abs/2007yCat.2276....0A>.
- J. Annis, M. Soares-Santos, M. A. Strauss, A. C. Becker, S. Dodelson, X. Fan, J. E. Gunn, J. Hao, Ž. Ivezić, S. Jester, L. Jiang, D. E. Johnston, J. M. Kubo, H. Lampeitl, H. Lin, R. H. Lupton, G. Miknaitis, H.-J. Seo, M. Simet, and B. Yanny. The sloan digital sky survey coadd: 275 deg² of deep Sloan Digital Sky Survey imaging on stripe 82. *ApJ*, 794:120, October 2014. doi: 10.1088/0004-637X/794/2/120. URL <http://adsabs.harvard.edu/abs/2014ApJ...794..120A>.
- S. Arnouts and O. Ilbert. Lephare: Photometric analysis for redshift estimate. Astrophysics Source Code Library, August 2011. URL <http://adsabs.harvard.edu/abs/2011ascl.soft08009A>.
- W. A. Baum. Photoelectric determinations of redshifts beyond 0.2 c. *AJ*, 62:6–7, February 1957. doi: 10.1086/107433. URL <http://adsabs.harvard.edu/abs/1957AJ.....62....6B>.
- N. Benítez. Bpz: Bayesian photometric redshift code. Astrophysics Source Code Library, August 2011. URL <http://adsabs.harvard.edu/abs/2011ascl.soft08011B>.

E. Bertin. Automated morphometry with sextractor and psfex. In I. N. Evans, A. Accomazzi, D. J. Mink, and A. H. Rots, editors, *Astronomical Data Analysis Software and Systems XX*, volume 442 of *Astronomical Society of the Pacific Conference Series*, page 435, July 2011. URL <http://adsabs.harvard.edu/abs/2011ASPC..442..435B>.

E. Bertin and S. Arnouts. Sextractor: Software for source extraction. *A&AS*, 117: 393–404, June 1996. doi: 10.1051/aas:1996164. URL <http://adsabs.harvard.edu/abs/1996A%26AS..117..393B>.

E. Bertin, Y. Mellier, M. Radovich, G. Missonnier, P. Didelon, and B. Morin. The terapix pipeline. In D. A. Bohlender, D. Durand, and T. H. Handley, editors, *Astronomical Data Analysis Software and Systems XI*, volume 281 of *Astronomical Society of the Pacific Conference Series*, page 228, 2002. URL <http://adsabs.harvard.edu/abs/2002ASPC..281..228B>.

R. Bielby, P. Hudelot, H. J. McCracken, O. Ilbert, E. Daddi, O. Le Fèvre, V. Gonzalez-Perez, J.-P. Kneib, C. Marmo, Y. Mellier, M. Salvato, D. B. Sanders, and C. J. Willott. The wircam deep survey. i. counts, colours, and mass-functions derived from near-infrared imaging in the cfhtls deep fields. *A&A*, 545:A23, September 2012. doi: 10.1051/0004-6361/201118547. URL <http://adsabs.harvard.edu/abs/2012A%26A...545A..23B>.

M. R. Blanton and S. Roweis. kcorrect: Calculate k-corrections between observed and desired bandpasses. Astrophysics Source Code Library, January 2017. URL <http://adsabs.harvard.edu/abs/2017ascl.soft01010B>.

M. Bolzonella, J.-M. Miralles, and R. Pelló. Hyperz: Photometric redshift code. Astrophysics Source Code Library, August 2011. URL <http://adsabs.harvard.edu/abs/2011ascl.soft08010B>.

R. J. Bouwens, G. D. Illingworth, R. I. Thompson, J. P. Blakeslee, M. E. Dickinson, T. J. Broadhurst, D. J. Eisenstein, X. Fan, M. Franx, G. Meurer, and P. van Dokkum. Star formation at $z \sim 6$: The hubble ultra deep parallel fields. *ApJ*, 606:L25–L28, May 2004a. doi: 10.1086/421016. URL <http://adsabs.harvard.edu/abs/2004ApJ...606L..25B>.

R. J. Bouwens, R. I. Thompson, G. D. Illingworth, M. Franx, P. G. van Dokkum, X. Fan, M. E. Dickinson, D. J. Eisenstein, and M. J. Rieke. Galaxies at $z \sim 7$ -8: z_{850} -dropouts in the hubble ultra deep field. *ApJ*, 616:L79–L82, December 2004b. doi: 10.1086/426503. URL <http://adsabs.harvard.edu/abs/2004ApJ...616L..79B>.

G. B. Brammer, P. G. van Dokkum, and P. Coppi. Eazy: A fast, public photometric redshift code. *ApJ*, 686:1503–1513, October 2008. doi: 10.1086/591786. URL <http://adsabs.harvard.edu/abs/2008ApJ...686.1503B>.

G. Bruzual and S. Charlot. Stellar population synthesis at the resolution of 2003. *MNRAS*, 344:1000–1028, October 2003. doi: 10.1046/j.1365-8711.2003.06897.x. URL <http://adsabs.harvard.edu/abs/2003MNRAS.344.1000B>.

K. Bundy, D. W. Hogg, T. D. Higgs, R. C. Nichol, N. Yasuda, K. L. Masters, D. Lang, and D. A. Wake. Synmag photometry: A fast tool for catalog-level matched colors of extended sources. *AJ*, 144:188, December 2012. doi: 10.1088/0004-6256/144/6/188. URL <http://adsabs.harvard.edu/abs/2012AJ....144..188B>.

K. Bundy, A. Leauthaud, S. Saito, A. Bolton, Y.-T. Lin, C. Maraston, R. C. Nichol, D. P. Schneider, D. Thomas, and D. A. Wake. The stripe 82 massive galaxy project. i. catalog construction. *ApJS*, 221:15, November 2015. doi: 10.1088/0067-0049/221/1/15. URL <http://adsabs.harvard.edu/abs/2015ApJS..221...15B>.

A. J. Bunker, E. R. Stanway, R. S. Ellis, and R. G. McMahon. The star formation rate of the universe at $z \sim 6$ from the hubble ultra-deep field. *MNRAS*, 355:374–384,

December 2004. doi: 10.1111/j.1365-2966.2004.08326.x. URL <http://adsabs.harvard.edu/abs/2004MNRAS.355..374B>.

- S. Carliles, T. Budavári, S. Heinis, C. Priebe, and A. Szalay. Photometric redshift estimation on sdss data using random forests. In R. W. Argyle, P. S. Bunclark, and J. R. Lewis, editors, *Astronomical Data Analysis Software and Systems XVII*, volume 394 of *Astronomical Society of the Pacific Conference Series*, page 521, August 2008. URL <http://adsabs.harvard.edu/abs/2008ASPC..394..521C>.
- A. A. Collister and O. Lahav. Annz: Estimating photometric redshifts using artificial neural networks. PASP, 116:345–351, April 2004. doi: 10.1086/383254. URL <http://adsabs.harvard.edu/abs/2004PASP..116..345C>.
- D. K. Erb, M. Pettini, A. E. Shapley, C. C. Steidel, D. R. Law, and N. A. Reddy. Physical conditions in a young, unreddened, low-metallicity galaxy at high redshift. ApJ, 719:1168–1190, August 2010. doi: 10.1088/0004-637X/719/2/1168. URL <http://adsabs.harvard.edu/abs/2010ApJ...719.1168E>.
- J. R. Graham and A. Dey. The redshift of an extremely red object and the nature of the very red galaxy population. ApJ, 471:720, November 1996. doi: 10.1086/178000. URL <http://adsabs.harvard.edu/abs/1996ApJ...471..720G>.
- J. E. Gunn, M. Carr, C. Rockosi, M. Sekiguchi, K. Berry, B. Elms, E. de Haas, Ž. Ivezić, G. Knapp, R. Lupton, G. Pauls, R. Simcoe, R. Hirsch, D. Sanford, S. Wang, D. York, F. Harris, J. Annis, L. Bartozek, W. Boroski, J. Bakken, M. Haldeman, S. Kent, S. Holm, D. Holmgren, D. Petravick, A. Protopiano, R. Rechenmacher, M. Doi, M. Fukugita, K. Shimasaku, N. Okada, C. Hull, W. Siegmund, E. Mannery, M. Blouke, D. Heidtman, D. Schneider, R. Lucinio, and J. Brinkman. The Sloan digital sky survey photometric camera. AJ, 116:3040–

3081, December 1998. doi: 10.1086/300645. URL <http://adsabs.harvard.edu/abs/1998AJ....116.3040G>.

E. M. Huff, C. M. Hirata, R. Mandelbaum, D. Schlegel, U. Seljak, and R. H. Lupton. Seeing in the dark - i. multi-epoch alchemy. *MNRAS*, 440:1296–1321, May 2014. doi: 10.1093/mnras/stu144. URL <http://adsabs.harvard.edu/abs/2014MNRAS.440.1296H>.

L. Jiang, X. Fan, F. Bian, J. Annis, K. Chiu, S. Jester, H. Lin, R. H. Lupton, G. T. Richards, M. A. Strauss, V. Malanushenko, E. Malanushenko, and D. P. Schneider. A survey of $z \sim 6$ quasars in the Sloan Digital Sky Survey Deep Stripe. ii. *AJ*, 138:305–311, July 2009. doi: 10.1088/0004-6256/138/1/305. URL <http://adsabs.harvard.edu/abs/2009AJ....138..305J>.

L. Jiang, X. Fan, F. Bian, I. D. McGreer, M. A. Strauss, J. Annis, Z. Buck, R. Green, J. A. Hodge, A. D. Myers, A. Rafiee, and G. Richards. The Sloan Digital Sky Survey Stripe 82 Imaging Data: Depth-Optimized Co-adds over 300 deg² in Five Filters. *ApJS*, 213:12, July 2014. doi: 10.1088/0067-0049/213/1/12. URL <http://adsabs.harvard.edu/abs/2014ApJS..213...12J>.

R. C. Kennicutt, Jr. The global Schmidt law in star-forming galaxies. *ApJ*, 498: 541–552, May 1998. doi: 10.1086/305588. URL <http://adsabs.harvard.edu/abs/1998ApJ...498..541K>.

M. Kriek, P. G. van Dokkum, I. Labb , M. Franx, G. D. Illingworth, D. Marchesini, R. F. Quadri, J. Aird, A. L. Coil, and A. Georgakakis. Fast: Fitting and assessment of synthetic templates. *Astrophysics Source Code Library*, March 2018. URL <http://adsabs.harvard.edu/abs/2018ascl.soft03008K>.

R. G. Kron. Photometry of a complete sample of faint galaxies. *ApJS*, 43:305–

- 325, June 1980. doi: 10.1086/190669. URL <http://adsabs.harvard.edu/abs/1980ApJS...43..305K>.
- P. Kroupa. On the variation of the initial mass function. MNRAS, 322:231–246, April 2001. doi: 10.1046/j.1365-8711.2001.04022.x. URL <http://adsabs.harvard.edu/abs/2001MNRAS.322..231K>.
- D. Lang. unwise: Unblurred coadds of the wise imaging. AJ, 147:108, May 2014. doi: 10.1088/0004-6256/147/5/108. URL <http://adsabs.harvard.edu/abs/2014AJ....147..108L>.
- S. J. Lilly, O. Le Fevre, F. Hammer, and D. Crampton. The canada-france redshift survey: The luminosity density and star formation history of the universe to z approximately 1. ApJ, 460:L1, March 1996. doi: 10.1086/309975. URL <http://adsabs.harvard.edu/abs/1996ApJ...460L...1L>.
- L. B. Lucy. An iterative technique for the rectification of observed distributions. AJ, 79:745, June 1974. doi: 10.1086/111605. URL <http://adsabs.harvard.edu/abs/1974AJ.....79..745L>.
- P. Madau and M. Dickinson. Cosmic star-formation history. ARA&A, 52:415–486, August 2014. doi: 10.1146/annurev-astro-081811-125615. URL <http://adsabs.harvard.edu/abs/2014ARA%26A..52..415M>.
- P. Madau, H. C. Ferguson, M. E. Dickinson, M. Giavalisco, C. C. Steidel, and A. Fruchter. High-redshift galaxies in the hubble deep field: colour selection and star formation history to $z \sim 4$. MNRAS, 283:1388–1404, December 1996. doi: 10.1093/mnras/283.4.1388. URL <http://adsabs.harvard.edu/abs/1996MNRAS.283.1388M>.
- A. Mainzer, J. Bauer, T. Grav, J. Masiero, R. M. Cutri, J. Dailey, P. Eisenhardt, R. S. McMillan, E. Wright, R. Walker, R. Jedicke, T. Spahr, D. Tholen, R. Alles,

- R. Beck, H. Brandenburg, T. Conrow, T. Evans, J. Fowler, T. Jarrett, K. Marsh, F. Masci, H. McCallon, S. Wheelock, M. Wittman, P. Wyatt, E. DeBaun, G. Elliott, D. Elsbury, T. Gautier, IV, S. Gomillion, D. Leisawitz, C. Maleszewski, M. Micheli, and A. Wilkins. Preliminary results from neowise: An enhancement to the wide-field infrared survey explorer for solar system science. *ApJ*, 731:53, April 2011. doi: 10.1088/0004-637X/731/1/53. URL <http://adsabs.harvard.edu/abs/2011ApJ...731...53M>.
- A. M. Meisner, D. Lang, and D. J. Schlegel. Deep full-sky coadds from three years of wise and neowise observations. *The Astronomical Journal*, 154(4):161, 2017. URL <http://stacks.iop.org/1538-3881/154/i=4/a=161>.
- E. Merlin, N. Bourne, M. Castellano, H. C. Ferguson, T. Wang, S. Derriere, J. S. Dunlop, D. Elbaz, and A. Fontana. T-phot version 2.0: Improved algorithms for background subtraction, local convolution, kernel registration, and new options. *Astronomy and Astrophysics*, 595:A97, November 2016. doi: 10.1051/0004-6361/201628751. URL <http://adsabs.harvard.edu/abs/2016A%26A...595A..97M>.
- D. J. Mink. Wcstools: an image astrometry toolkit. In *AAS/Division of Dynamical Astronomy Meeting*, volume 30 of *Bulletin of the American Astronomical Society*, page 1144, September 1998. URL <http://adsabs.harvard.edu/abs/1998DDA...29.0806M>.
- J. Moustakas, A. L. Coil, J. Aird, M. R. Blanton, R. J. Cool, D. J. Eisenstein, A. J. Mendez, K. C. Wong, G. Zhu, and S. Arnouts. Primus: Constraints on star formation quenching and galaxy merging, and the evolution of the stellar mass function from $z = 0\text{--}1$. *ApJ*, 767:50, April 2013. doi: 10.1088/0004-637X/767/1/50. URL <http://adsabs.harvard.edu/abs/2013ApJ...767...50M>.
- M. Musin and H. Yan. Synergy of wise and sdss in stripe 82. *in press.*, in prep.

- A. Muzzin, D. Marchesini, M. Stefanon, M. Franx, H. J. McCracken, B. Milvang-Jensen, J. S. Dunlop, J. P. U. Fynbo, G. Brammer, I. Labb , and P. G. van Dokkum. The evolution of the stellar mass functions of star-forming and quiescent galaxies to $z = 4$ from the cosmo/ultravista survey. *ApJ*, 777:18, November 2013. doi: 10.1088/0004-637X/777/1/18. URL <http://adsabs.harvard.edu/abs/2013ApJ...777...18M>.
- M. Negrello, S. Serjeant, C. Pearson, T. Takagi, A. Efstathiou, T. Goto, D. Burgarella, W.-S. Jeong, M. Im, H. M. Lee, H. Matsuhara, S. Oyabu, T. Wada, and G. White. Photometric redshift accuracy in akari deep surveys. *MNRAS*, 394:375–397, March 2009. doi: 10.1111/j.1365-2966.2008.14293.x. URL <http://adsabs.harvard.edu/abs/2009MNRAS.394..375N>.
- G. Neugebauer, H. J. Habing, R. van Duinen, H. H. Aumann, B. Baud, C. A. Beichman, D. A. Beintema, N. Boggess, P. E. Clegg, T. de Jong, J. P. Emerson, T. N. Gautier, F. C. Gillett, S. Harris, M. G. Hauser, J. R. Houck, R. E. Jennings, F. J. Low, P. L. Marsden, G. Miley, F. M. Olmon, S. R. Pottasch, E. Raimond, M. Rowan-Robinson, B. T. Soifer, R. G. Walker, P. R. Wesselius, and E. Young. The infrared astronomical satellite (iras) mission. *ApJ*, 278:L1–L6, March 1984. doi: 10.1086/184209. URL <http://adsabs.harvard.edu/abs/1984ApJ...278L...1N>.
- C. Papovich, H. V. Shipley, N. Mehrtens, C. Lanham, M. Lacy, R. Ciardullo, S. L. Finkelstein, R. Bassett, P. Behroozi, G. A. Blanc, R. S. de Jong, D. L. DePoy, N. Drory, E. Gawiser, K. Gebhardt, C. Gronwall, G. J. Hill, U. Hopp, S. Jodgee, L. Kawinwanichakij, J. L. Marshall, E. McLinden, E. Mentuch Cooper, R. S. Somerville, M. Steinmetz, K.-V. Tran, S. Tuttle, M. Viero, R. Wechsler, and G. Zeimann. The spitzer-hetdex exploratory large-area survey. *ApJS*, 224:28, June 2016. doi: 10.3847/0067-0049/224/2/28. URL <http://adsabs.harvard.edu/abs/2016ApJS..224...28P>.

- W. D. Pence, L. Chiappetti, C. G. Page, R. A. Shaw, and E. Stobie. Definition of the flexible image transport system (fits), version 3.0. *Astronomy and Astrophysics*, 524:A42, December 2010. doi: 10.1051/0004-6361/201015362. URL <http://adsabs.harvard.edu/abs/2010A&26A...524A..42P>.
- W. H. Richardson. Bayesian-based iterative method of image restoration. *Journal of the Optical Society of America (1917-1983)*, 62:55, January 1972. URL <http://adsabs.harvard.edu/abs/1972JOSA...62...55R>.
- M. Rowan-Robinson, T. Babbedge, S. Oliver, M. Trichas, S. Berta, C. Lonsdale, G. Smith, D. Shupe, J. Surace, S. Arnouts, O. Ilbert, O. Le Févre, A. Afonso-Luis, I. Perez-Fournon, E. Hatziminaoglou, M. Polletta, D. Farrah, and M. Vacari. Photometric redshifts in the swire survey. *MNRAS*, 386:697–714, May 2008. doi: 10.1111/j.1365-2966.2008.13109.x. URL <http://adsabs.harvard.edu/abs/2008MNRAS.386..697R>.
- E. Rozo, E. S. Rykoff, M. Becker, R. M. Reddick, and R. H. Wechsler. redmapper - iv. photometric membership identification of red cluster galaxies with 1 per cent precision. *MNRAS*, 453:38–52, October 2015. doi: 10.1093/mnras/stv1560. URL <http://adsabs.harvard.edu/abs/2015MNRAS.453...38R>.
- E. S. Rykoff, E. Rozo, M. T. Busha, C. E. Cunha, A. Finoguenov, A. Evrard, J. Hao, B. P. Koester, A. Leauthaud, B. Nord, M. Pierre, R. Reddick, T. Sadibekova, E. S. Sheldon, and R. H. Wechsler. redmapper. i. algorithm and sdss dr8 catalog. *ApJ*, 785:104, April 2014. doi: 10.1088/0004-637X/785/2/104. URL <http://adsabs.harvard.edu/abs/2014ApJ...785..104R>.
- E. E. Salpeter. The luminosity function and stellar evolution. *ApJ*, 121:161, January 1955. doi: 10.1086/145971. URL <http://adsabs.harvard.edu/abs/1955ApJ...121..161S>.

- M. Schmidt. The rate of star formation. *ApJ*, 129:243, March 1959. doi: 10.1086/146614. URL <http://adsabs.harvard.edu/abs/1959ApJ...129..243S>.
- R. F. Silverberg, M. G. Hauser, N. W. Boggess, T. J. Kelsall, S. H. Moseley, and T. L. Murdock. Design of the diffuse infrared background experiment (dirbe) on cobe. In M. S. Scholl, editor, *Infrared Spaceborne Remote Sensing*, volume 2019 of Proc. SPIE, pages 180–189, October 1993. doi: 10.1117/12.157825. URL <http://adsabs.harvard.edu/abs/1993SPIE.2019..180S>.
- J. Singal, M. Shmakova, B. Gerke, R. L. Griffith, and J. Lotz. The efficacy of galaxy shape parameters in photometric redshift estimation: A neural network approach. *PASP*, 123:615, May 2011. doi: 10.1086/660155. URL <http://adsabs.harvard.edu/abs/2011PASP..123..615S>.
- S. A. Smee, R. H. Barkhouser, G. A. Scharfstein, M. Meixner, J. D. Orndorff, and T. Miller. Design of the wiyn high resolution infrared camera (whirc). *PASP*, 123: 87, January 2011. doi: 10.1086/658238. URL <http://adsabs.harvard.edu/abs/2011PASP..123...87S>.
- SAO Staff. Smithsonian astrophysical observatory star catalog. *Smithsonian publ. 4652*, 1966.
- M. B. Taylor. Stilts - a package for command-line processing of tabular data. In C. Gabriel, C. Arviset, D. Ponz, and S. Enrique, editors, *Astronomical Data Analysis Software and Systems XV*, volume 351 of *Astronomical Society of the Pacific Conference Series*, page 666, July 2006. URL <http://adsabs.harvard.edu/abs/2006ASPC..351..666T>.
- J. Walcher, B. Groves, T. Budavári, and D. Dale. Fitting the integrated spectral energy distributions of galaxies. *Ap&SS*, 331:1–52, January 2011. doi: 10.1007/

s10509-010-0458-z. URL <http://adsabs.harvard.edu/abs/2011Ap%26SS.331....1W>.

E. L. Wright, P. R. M. Eisenhardt, A. K. Mainzer, M. E. Ressler, R. M. Cutri, T. Jarrett, J. D. Kirkpatrick, D. Padgett, R. S. McMillan, M. Skrutskie, S. A. Stanford, M. Cohen, R. G. Walker, J. C. Mather, D. Leisawitz, T. N. Gautier, III, I. McLean, D. Benford, C. J. Lonsdale, A. Blain, B. Mendez, W. R. Irace, V. Duval, F. Liu, D. Royer, I. Heinrichsen, J. Howard, M. Shannon, M. Kendall, A. L. Walsh, M. Larsen, J. G. Cardon, S. Schick, M. Schwalm, M. Abid, B. Fabinsky, L. Naes, and C.-W. Tsai. The wide-field infrared survey explorer (wise): Mission description and initial on-orbit performance. AJ, 140:1868-1881, December 2010. doi: 10.1088/0004-6256/140/6/1868. URL <http://adsabs.harvard.edu/abs/2010AJ....140.1868W>.

L. Yan, D. Thompson, and B. T. Soifer. Optical spectroscopy of k-selected extremely red galaxies. AJ, 127:1274–1284, March 2004. doi: 10.1086/382098. URL <http://adsabs.harvard.edu/abs/2004AJ....127.1274Y>.

D. G. York, J. Adelman, J. E. Anderson, Jr., S. F. Anderson, J. Annis, N. A. Bahcall, J. A. Bakken, R. Barkhouser, S. Bastian, E. Berman, W. N. Boroski, S. Bracker, C. Briegel, J. W. Briggs, J. Brinkmann, R. Brunner, S. Burles, L. Carey, M. A. Carr, F. J. Castander, B. Chen, P. L. Colestock, A. J. Connolly, J. H. Crocker, I. Csabai, P. C. Czarapata, J. E. Davis, M. Doi, T. Dombeck, D. Eisenstein, N. Ellman, B. R. Elms, M. L. Evans, X. Fan, G. R. Federwitz, L. Fiscelli, S. Friedman, J. A. Frieman, M. Fukugita, B. Gillespie, J. E. Gunn, V. K. Gurbani, E. de Haas, M. Haldeman, F. H. Harris, J. Hayes, T. M. Heckman, G. S. Hennessy, R. B. Hindley, S. Holm, D. J. Holmgren, C.-h. Huang, C. Hull, D. Husby, S.-I. Ichikawa, T. Ichikawa, Ž. Ivezić, S. Kent, R. S. J. Kim, E. Kinney, M. Klaene, A. N. Kleinman, S. Kleinman, G. R. Knapp, J. Korieneck, R. G. Kron, P. Z. Kunszt,

D. Q. Lamb, B. Lee, R. F. Leger, S. Limmongkol, C. Lindenmeyer, D. C. Long, C. Loomis, J. Loveday, R. Lucinio, R. H. Lupton, B. MacKinnon, E. J. Mannery, P. M. Mantsch, B. Margon, P. McGehee, T. A. McKay, A. Meiksin, A. Merelli, D. G. Monet, J. A. Munn, V. K. Narayanan, T. Nash, E. Neilsen, R. Neswold, H. J. Newberg, R. C. Nichol, T. Nicinski, M. Nonino, N. Okada, S. Okamura, J. P. Ostriker, R. Owen, A. G. Pauls, J. Peoples, R. L. Peterson, D. Petravick, J. R. Pier, A. Pope, R. Pordes, A. Prosapio, R. Rechenmacher, T. R. Quinn, G. T. Richards, M. W. Richmond, C. H. Rivetta, C. M. Rockosi, K. Ruthmansdorfer, D. Sandford, D. J. Schlegel, D. P. Schneider, M. Sekiguchi, G. Sergey, K. Shimasaku, W. A. Siegmund, S. Smee, J. A. Smith, S. Snedden, R. Stone, C. Stoughton, M. A. Strauss, C. Stubbs, M. SubbaRao, A. S. Szalay, I. Szapudi, G. P. Szokoly, A. R. Thakar, C. Tremonti, D. L. Tucker, A. Uomoto, D. Vandenberg, M. S. Vogeley, P. Waddell, S.-i. Wang, M. Watanabe, D. H. Weinberg, B. Yanny, N. Yasuda, and SDSS Collaboration. The Sloan Digital Sky Survey: Technical summary. *AJ*, 120:1579–1587, September 2000. doi: 10.1086/301513. URL <http://adsabs.harvard.edu/abs/2000AJ....120.1579Y>.